Acta Pharmaceutica Sinica B 2022;12(5):2533–2549

Chinese Pharmaceutical Association
Institute of Materia Medica, Chinese Academy of Medical Sciences

Acta Pharmaceutica Sinica B

www.elsevier.com/locate/apsb
www.sciencedirect.com

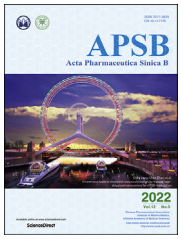

ORIGINAL ARTICLE

Stimuli-responsive nano vehicle enhances cancer immunotherapy by coordinating mitochondria-targeted immunogenic cell death and PD-L1 blockade

Qiuyi Li, Cheng Chen, Jinxia Kong, Lian Li, Junlin Li, Yuan Huang*

Key Laboratory of Drug-Targeting and Drug Delivery System of the Education Ministry and Sichuan Province, Sichuan Engineering Laboratory for Plant-Sourced Drug and Sichuan Research Center for Drug Precision Industrial Technology, West China School of Pharmacy, Sichuan University, Chengdu 610041, China

Received 23 July 2021; received in revised form 3 October 2021; accepted 20 October 2021

KEY WORDS

Immunogenic cell death;
Mitochondrial targeting;
PD-L1 blockade;
Endoplasmic reticulum stress;
Mitochondria-associated damage molecules;
Stimuli-responsive;
Antitumor immune responses;
Antitumor efficacy

Abstract Induction of immunogenic cell death promotes antitumor immunity against cancer. However, majority of clinically-approved drugs are unable to elicit sufficient ICD. Here, our study revealed that mitochondria-targeted delivery of doxorubicin (DOX) massively amplified ICD *via* substantial generation of reactive oxygen species (ROS) after mitochondrial damage. The underlying mechanism behind increased ICD was further demonstrated to be ascribed to two pathways: (1) ROS elevated endoplasmic reticulum (ER) stress, leading to surface exposure of calreticulin; (2) ROS promoted release of various mitochondria-associated damage molecules including mitochondrial transcription factor A. Nevertheless, adaptive upregulation of PD-L1 was found after such ICD-inducing treatment. To overcome such immunosuppressive feedback, we developed a tumor stimuli-responsive nano vehicle to simultaneously exert mitochondrial targeted ICD induction and PD-L1 blockade. The nano vehicle was self-assembled from ICD-inducing copolymer and PD-L1 blocking copolymer, and possessed long-circulating property which contributed to better tumor accumulation and mitochondrial targeting. As a result, the nano vehicle remarkably activated antitumor immune responses and exhibited robust antitumor efficacy in both immunogenic and non-immunogenic tumor mouse models.

*Corresponding author. Tel./fax: +86 28 85501617.
E-mail address: huangyuan0@163.com (Yuan Huang).

Peer review under responsibility of Chinese Pharmaceutical Association and Institute of Materia Medica, Chinese Academy of Medical Sciences.

https://doi.org/10.1016/j.apsb.2021.11.005

1. Introduction

Since one important hallmark of tumor is immune surveillance evasion, immunogenic cell death (ICD) has emerged as an attractive strategy for tumor immunotherapy[1–3]. Apoptotic cells undergoing elevated endoplasmic reticulum (ER) stress could render induction of damage-associated molecular patterns (DAMPs), such as surface exposure of calreticulin (CRT) and extracellular release of high mobility group protein B1 (HMGB1), resulting in facilitated phagocytosis by antigen-presenting cells (APCs) and killing effect of T cells[3,4]. However, majority of clinically-approved drugs are unable to trigger sufficient ICD, making the application of ICD restricted. Notably, oxidative stress is closely associated with ICD. Evidences showed that stimulating production of intracellular reactive oxygen species (ROS) could evoke abundant ICD, which immensely broadened the applicability of ICD[4–6].

Mitochondria are vital metabolic organelles participating adenosine triphosphate (ATP) production and intrinsic cell apoptosis[7]. As mitochondria are the main resource of cellular ROS, studies demonstrated that mitochondrial targeted oxidative stress was capable of disrupting ER homeostasis to trigger ER stress, subsequently eliciting massive ICD[8–10]. In addition, damaged mitochondria could secrete mitochondria-associated damage molecules, *e.g.*, ATP and mitochondrial transcription factor A (TFAM), an analogue of HMGB1, to improve immune recognition and ICD efficacy[11–13]. Accordingly, we speculate that mitochondria would be an attractive target for efficient ICD induction. Anthracycline drugs, *e.g.*, doxorubicin and epirubicin, were known to induce mild ICD *via* secondary effect. However, whether targeted delivery of these chemotherapeutics to mitochondria could trigger stronger ICD and the underlying mechanism is unknown. In our previous study, we developed a mitochondrial targeted hybrid peptide-decorated *N*-(2-hydroxypropyl) methacrylamide (HPMA) copolymer–doxorubicin conjugate (P-D-R8MTS), which could remarkably increase mitochondrial accumulation of doxorubicin (DOX) and intracellular ROS level[14]. In this work, we firstly demonstrated that P-D-R8MTS was more capable to induce ICD by promoting DAMPs release compared with non-mitochondrial targeted HPMA copolymer-doxorubicin conjugate (PD). This suggested P-D-R8MTS might be a promising ICD inducer. Nevertheless, the cationic charge of P-D-R8MTS tremendously impeded its *in vivo* circulation and tumor accumulation.

Moreover, after chemotherapeutics treatment, tumor cells could adaptively upregulate PD-L1 expression, which further aggravates immunosuppressive environment and impedes infiltration and activation of effector T cells[15,16]. Therefore, simultaneously increasing immune-stimulation and relieving immunosuppression is crucial for efficient immunotherapy. Inspired by the advantages of low adverse effect and low

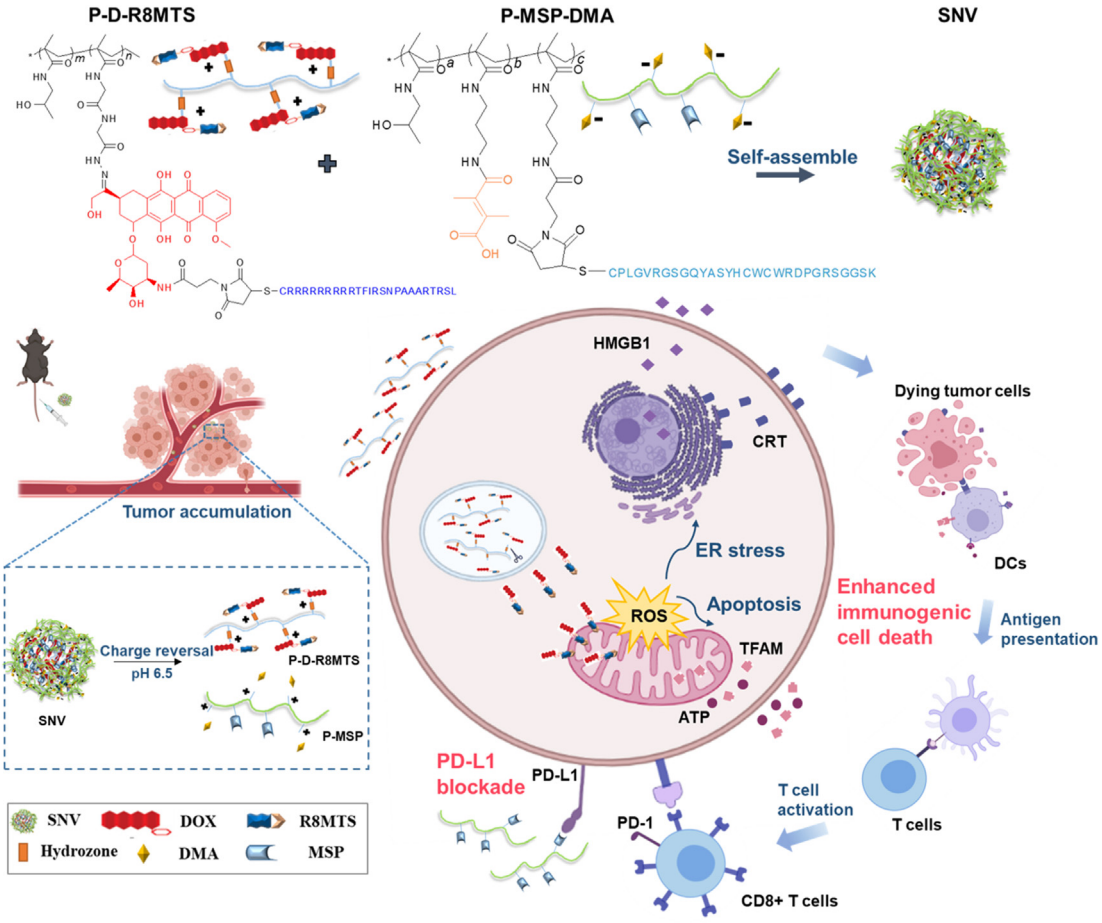

Scheme 1 Schematic illustration of the self-assembled nano vehicle (SNV) consisting of mitochondrial targeted ICD induction and PD-L1 blocking to activate immunity for cancer immunotherapy.

production cost, PD-L1 antagonistic peptide has been evolved as a potential candidate to interact with PD-L1 for PD-1/PD-L1 checkpoint blockade[17,18].

HPMA copolymer is a water-soluble nanocarrier with advantages of biocompatibility and long-circulating effect owning to the high molecular weight (Mw) and hydrophilic nature[19,20]. Here, we established a novel tumor stimuli-responsive self-assembled nano vehicle (SNV) consisting of cationic mitochondrial targeted ICD inducer (P-D-R8MTS) and anionic PD-L1 blocking copolymer (P-MSP-DMA). PD-L1 antagonistic peptide MSP was conjugated to HPMA copolymers, and then modified with dimethylmaleic anhydride (DMA) to self-assemble with P-D-R8MTS *via* electrostatic interaction. Our results showed that SNV possessed prolonged circulating property and enhanced tumor accumulation. Once reaching tumor acidic microenvironment, DMA would be detached from P-MSP-DMA and SNV disassembled. Afterwards, P-D-R8MTS targeted tumor mitochondria to induce ROS generation, which elicited mitochondrial dysfunction and ER stress, resulting in amplified ICD. Meanwhile, P-MSP bound to PD-L1 to block PD-1/PD-L1 interaction and unleash the killing effect of $CD8^+$ T cells. By these efforts, the multifunctional SNV potentiated antitumor immunity in both immunogenic B16F10 melanoma and non-immunogenic 4T1 breast cancer *via* mitochondrial targeted ICD induction and immunosuppressive mitigation (Scheme 1).

2. Materials and methods

2.1. Materials

Doxorubicin hydrochloride (DOX·HCl), indirubin-3′-oxime (DiR), cyanine5 (Cy5) and cyanine3 (Cy3) were purchased from Dalian Meilun Biotech Co., Ltd. (Dalian, China). Cell penetrating peptide (R8: RRRRRRRRC) and mitochondrial targeting chimeric peptide (R8MTS: LSRTRAAAPNSRIFTRRRRRRRRRC) were synthesized by Apeptide Co., Ltd. (Shanghai, China). PD-L1 antagonistic peptide (MSP: CPLGVRGSGQYASYHCWCWRDPGRSGGSK) was synthesized by China Peptides Co., Ltd. (Shanghai, China). Glycylglycine (GG), 2,3-dimethylmaleic anhydride (DMA) and *N*-succinimidyl-3-maleimidopropionate (SMP) were purchased from J&K Co. Ltd. (Shanghai, China). 3-(4, 5-Dimethyl-2-tetrazolyl)-2,5-diphenyl-2*H* tetrazoliumbromide (MTT), 4′,6-diamidino-2-phenylindole (DAPI) were purchased from Sigma−Aldrich (St. Louis, MO, USA). Cell-tracer Green (CMFDA), mitotracker Green, enhanced BCA protein assay Kit, reactive oxygen species assay kit, mitochondrial permeability transition pores assay kit and tissue mitochondria isolation kit, anti-TFAM, anti-HMGB1, anti-GRP78 and anti-P-ELF2α were purchased from Beyotime Biotechnology (Shanghai, China). Anti-CRT antibody, anti-CHOP antibody and Alexa Fluor 647-conjugated second antibody were purchased from Abcam (Cambridge, UK). APC annexin V apoptosis detection kit with 7-AAD, anti-CD45-PerCP/Cy5.5, anti-CD3-FITC, anti-CD8-APC, anti-CD4-PerCP, anti-CD274-PE, anti-CD274-APC, anti-CD11C-APC, anti-CD11C-FITC, anti-CD80-APC and anti-CD86-PerCP/Cy5.5 antibodies were purchased from Biolegend (San Diego, CA, USA). Anti-CD16/32, CD8-depletion antibody, anti-FOXP3-PE antibodies, transcription factor buffer set were purchased from BD Biosciences (Bedford, MA, USA). *N*-(3-Aminopropyl) methacrylamide (APMA) was purchased from Bide Pharmatech Ltd. (Shanghai, China). The rabbit anti-actin primary antibodies and HRP-labelled goat anti-rabbit secondary antibodies were purchased from Servicebio (Wuhan, China). *N*-(2-Hydroxypropyl) methacrylamide (HPMA) and *N*-methacryloylglycylglycyl-hydrazide-doxorubicin (MA-GG-NHN=DOX) were synthesized according to previous studies[21,22]. Mouse melanoma cell line B16F10 and breast cancer cell line 4T1 were purchased from the Cell Bank of Chinese Academy of Sciences (Shanghai, China).

2.2. Synthesis and characterization of mitochondrial targeted HPMA copolymer-DOX conjugate and PD-L1 antagonistic HPMA copolymer

The mitochondrial targeting chimeric peptide modified HPMA copolymer-DOX conjugate (P-D-R8MTS) was synthesized as previously reported[14]. Briefly, the HPMA copolymer-DOX conjugates (PD) were firstly synthesized through radical solution copolymerization in methanol (HPMA and MA-GG-NHN=DOX at a molar ratio of 92.5:7.5, comonomers:azodiisobutyronitrile (AIBN):methanol = 12.5:2:85.5, wt%). In details, HPMA (200.00 mg, 1.40 mmol), MA-GG-NHN=DOX (84.03 mg, 0.11 mmol) and AIBN (45.44 mg) were dissolved in 2.5 mL methanol. The copolymerization was carried out in sealed ampoules at 50 °C under argon atmosphere. After 24 h, the solvent was precipitated in the mixture of diethyl ether and acetone (diethyl ether:acetone = 3:1). The precipitations were dissolved in deionized water, dialyzed and lyophilized to obtain PD. Then PD (100.00 mg) and *N*-succinimidyl-3-maleimidopropionate (SMP, 15.87 mg) were reacted in dimethylformamide (DMF, 6 mL) for 24 h. The solvent was dialyzed against deionized water for 48 h and lyophilized to obtain P-D-SMP. Finally, P-D-SMP (100.00 mg) and R8MTS peptide (40.00 mg) were dissolved in phosphate buffer saline solution (PBS, pH 7.0, 6 mL) with the protection of argon, stirred at room temperature for 48 h, then dialyzed at 4 °C, and lyophilized to obtain P-D-R8MTS. P-D-R8 was synthesized *via* the same method. For cyanine5 (Cy5)-labeled HPMA copolymer-DOX conjugate, P-A-D was firstly synthesized at a molar ratio of HPMA:APMA:MA-GG-NHN=DOX = 90.5:2:7.5. In details, HPMA (100.00 mg, 0.70 mmol), APMA (2.76 mg, 0.02 mmol), MA−GG−NHN=DOX (42.84 mg, 0.06 mmol) and AIBN (23.30 mg) were dissolved in 1.3 mL methanol. The copolymerization was carried out in sealed ampoules at 50 °C under argon atmosphere. Then Cy5 (1.83 mg) was reacted with P-A-D (50.00 mg) in PBS (3 mL) for 4 h to obtain P-D-Cy5. After that, SMP attachment and R8MTS peptide decoration were using the same method mentioned above to obtain P-D-R8MTS-Cy5.

PD-L1 antagonistic HPMA copolymer with charge shielding was synthesized in four steps. Firstly, HPMA copolymer with cationic amino groups (P-A) was synthesized *via* radical solution copolymerization at a molar ratio of HPMA:APMA = 80%:20%. In details, HPMA (200.00 mg, 1.40 mmol), APMA (62.36 mg, 0.35 mmol) and AIBN (41.92 mg) were dissolved in 2.3 mL methanol. The copolymerization was carried out in sealed ampoules at 50 °C under argon atmosphere. After 24 h, the solvent was precipitated in the mixture of diethyl ether and acetone (diethyl ether:acetone = 3:1). The precipitations were dissolved in deionized water, dialyzed and lyophilized to obtain PA. Then PA (100.00 mg) and SMP (15.00 mg) were reacted in dimethylformamide (DMF, 6 mL) at 50 °C for 24 h. The solvent was dialyzed against deionized water for 48 h and lyophilized to obtain P-A-SMP. After that, P-A-SMP (100.00 mg) and MSP peptide

(40.00 mg) were dissolved in PBS (pH 7.0, 6 mL) with the protection of argon, stirred at room temperature for 48 h, then dialyzed at 4 °C, and lyophilized to obtain P-A-MSP. Finally, P-A-MSP (100.00 mg) was dissolved in 0.1 mol/L sodium bicarbonate buffer (6 mL), and 2,3-dimethylmaleic anhydride (DMA, 15 mg) was added slowly. The pH was maintained in the range of 8.5−9.0 during the whole process. After 4 h reaction, the solution was dialyzed against 0.1 mol/L sodium bicarbonate buffer for 24 h and deionized water for another 12 h, and lyophilized to obtain P-MSP-DMA. For Cy5 and cyanine3 (Cy3)-labeled HPMA copolymer-DOX conjugate, P-A was firstly synthesized as the same method. Then Cy5 (1.22 mg) and Cy3 (1.22 mg) was reacted with P-A-D (50.00 mg) for 4 h to obtain P-A-Cy5 and P-A-Cy3, respectively. After that, SMP attachment and MSP peptide decoration were using the same method mentioned above to obtain P-MSP-DMA-Cy5 and P-MSP-DMA-Cy3.

^{1}H NMR spectra were applied to determine the structure of P-D-R8MTS and P-MSP-DMA. The molecular weight and polydispersity index (PDI) were measured by fast protein liquid chromatography system (AKTA purifier, GE Healthcare, NJ, USA) with a Superose 6 10/300 GL analytical column (GE Healthcare, NJ, USA). The mobile phase was phosphate buffer solution (pH 7.4, NaH_2PO_4 1.50 g/L, Na_2HPO_4 14.50 g/L, NaCl 8.76 g/L) with the flow rate of 0.5 mL/min. The size and zeta potential of each HPMA copolymer conjugate were measured by Zetasizer Nano-ZS90 (Malvern Instruments Ltd., Malvern, UK). The DOX content was determined by UV−Vis spectroscopy (Evolution 300, Thermo Fisher Scientific, MA, USA) at 484 nm. The peptide content was detected by amino acid analysis (Commonwealth Biotech, VA, USA) and Enhanced BCA Protein Assay Kit (Beyotime Biotechnology, Shanghai, China).

2.3. Preparation and characterization of self-assembled nano vehicle

The self-assembled nano vehicle (SNV) was prepared *via* cross-linking of P-D-R8MTS and P-MSP-DMA. Two copolymer conjugates (P-D-R8MTS:P-MSP-DMA = 1:2, *w*/*w*) were separately dissolved in deionized water, and then P-MSP-DMA was added into P-D-R8MTS solution dropwise under stirring for 10 min.

The size and zeta potential of SNV were measured by Zetasizer Nano-ZS90. For serum stability analysis of SNV, SNV (1 mg/mL) was dissolved in PBS containing 50% fetal bovine serum. At predetermined time points (0, 1, 2, 4, 6, 8, and 24 h), the size and zeta potential were monitored by Zetasizer Nano-ZS90. To investigate the morphology of SNV, SNV (1 mg/mL) was incubated in different pH (6.5 and 7.4) for 2 h and then analyzed by transmission electron microscopy (Hitachi H600, Tokyo, Japan). For charge reversal of P-MSP-DMA, P-MDP-DMA (1 mg/mL) was dissolved in different pH (pH 6.5 and 7.4), At predetermined time points (0, 1, 2, 4, 6, and 8 h), the zeta potential was monitored by Zetasizer Nano-ZS90.

To investigate the drug release profile of P-D-R8MTS and SNV under different pH (pH 7.4, 6.5, and 5.0), P-D-R8MTS and SNV were dissolved in above phosphate buffer (equivalent DOX concentration: 3 mg/mL). Then, 1.5 mL of P-D-R8MTS and SNV solutions were dialyzed in 30 mL of corresponding phosphate buffer (37 °C, pH 7.4, 6.5 and 5.0). At predetermined time points (0.5, 1, 2, 4, 6, 8, 12, 24, and 48 h), 100 μL of external solution was collected and replaced with corresponding fresh phosphate buffer. The fluorescence intensity of DOX was measured by Varioskan Flash (E_{ex} = 535 nm, E_{em} = 590 nm, ThermoFisher Scientific, MA, USA). Each assay was repeated in triplicate.

2.4. Cell culture and animal models

Mouse melanoma cell line B16F10 and breast cancer cell line 4T1 were cultured in RPMI-1640 medium supplemented with 10% fetal bovine serum and 1% antibiotics (penicillin and streptomycin). Cells were incubated at 37 °C with 5% CO_2.

Female C57/BL6 mice and BALB/c mice (4−6 weeks) were purchased from Dashuo Biological Technology (Chengdu, China). All the animal experiments were executed according to the protocols approved by Sichuan University.

2.5. Cellular uptake and subcellular distribution

For cellular uptake, B16F10 cells (1×10^5 cells/well) were seeded onto 12-well plates and incubated with PD, P-D-R8, P-D-R8MTS, SNV (pH 7.4 and 6.5) for 1 or 4 h (equivalent DOX concentration 10 μg/mL). Cells were harvested and analyzed by flow cytometry (Beckman CytoFLEX S, Brea, CA, USA). To investigate the uptake mechanism of P-D-R8MTS and SNV in B16F10 cells, cells were seeded onto 12-well plates and pretreated with various inhibitors including active transport inhibitor sodium azide (NaN_3, 1 mg/mL), clathrin-mediated endocytosis inhibitor chlorpromazine (10 μg/mL), caveolae-mediated endocytosis inhibitor lovastatin (10 μg/mL) and macropinocytosis inhibitor amiloride (0.3 mg/mL) for 1 h. Then the medium was removed and cells were incubated with P-D-R8MTS and SNV (pH 7.4 and 6.5) for another 4 h. Cells were collected and the fluorescence intensity was analyzed by flow cytometry.

For analysis of SNV disassembly at pH 6.5, B16F10 cells (5×10^4 cells/well) were seeded onto glass coverslips and incubated with SNV (self-assembled from P-D-R8MTS and P-MSP-DMA-Cy5, equivalent DOX concentration 10 μg/mL) for 1 and 4 h. Then, cells were washed, fixed with 4% paraformaldehyde and stained with DAPI (5 μg/mL) for 4 min. The fluorescence images were analyzed by confocal laser scanning microscopy (CLSM, Zeiss LSM 800, Oberkochen, Germany).

For subcellular distribution, the mitochondria of B16F10 cells were extracted to evaluate the accumulation of DOX. Briefly, B16F10 cells treated with PD, P-D-R8, P-D-R8MTS and SNV (pH 7.4 and 6.5) for 4 h were collected and incubated with mitochondrial extraction reagent (Tris base 10 mmol/L, NaCl 10 mmol/L, $MgCl_2$ 25 mmol/L) at 4 °C for 10 min, and then cells were homogenized for twenty times. The suspensions were centrifuged (600×*g*, 10 min, ZONKIA KDC-140HR), and then the supernatant was collected and centrifuged (11,000×*g*, 10 min). The precipitates were suspended with PBS and immediately measured by flow cytometry. For qualitative analysis, B16F10 and 4T1 cells (5×10^4 cells/well) were seeded onto glass coverslips and incubated with above drugs for 4 h. Then, cells were washed and stained with Mito-tracker Green (100 nmol/L) for 45 min. After that, cells were washed, fixed with 4% paraformaldehyde and stained with DAPI (5 μg/mL) for 4 min. The fluorescence images were analyzed by CLSM.

2.6. Evaluation of mitochondrial dysfunction

ROS generation was measured by using 2′,7′-dichlorofluorescein diacetate (DCFH DA). B16F10 and 4T1 cells were treated with drugs (equivalent DOX concentration 10 μg/mL) for 12 h. Then cells were collected and incubated with 10 μmol/L DCFH DA for 30 min. After that, cells were washed twice and analyzed by flow

cytometry. The fluorescence intensity represented the intracellular ROS level.

To investigate the opening of mitochondrial permeability transition pores (MPTPs), B16F10 cells were treated with P-D-R8MTS, P-MSP-DMA (pH 7.4 and 6.5) and SNV (pH 7.4 and 6.5) for 12 h (equivalent DOX concentration 10 μg/mL). Then cells were collected and incubated with fluorescence quenching solution containing calcein AM and $CoCl_2$ at 37 °C for 30 min. Cells were washed and analyzed by flow cytometry.

2.7. Evaluation of ER stress

To investigate the ER stress, B16F10 cells were treated with PD, P-D-R8, P-D-R8MTS, P-MSP-DMA (pH 7.4 and 6.5) and SNV (pH 7.4 and 6.5) for 24 h (equivalent DOX concentration 10 μg/mL). After that, cells were blocked with 5% goat serum for 20 min, fixed and permeabilized by Transcription Factor Buffer Set, and then incubated with anti-CHOP antibody (1:500 dilution), anti-GPR78 antibody (1:100 dilution) and anti- P-ELF2α antibody (1:100 dilution) at 4 °C for 1 h and Alexa Fluor 647-conjugated second antibody (1:500 dilution) at room temperature for 45 min. Cells were washed and immediately analyzed by flow cytometry.

2.8. Induction of immunogenic cell death

To investigate the ecto-CRT on cell surface, B16F10 cells and 4T1 cells were treated with PD, P-D-R8, P-D-R8MTS, P-MSP-DMA (pH 7.4 and 6.5) and SNV (pH 7.4 and 6.5) for 24 h (equivalent DOX concentration 10 μg/mL). After that, cells were blocked with 5% goat serum for 20 min, and then incubated with anti-CRT antibody (1:500 dilution) at 4 °C for 1 h and Alexa Fluor 647-conjugated second antibody (1:500 dilution) at room temperature for 45 min. Cells were washed and immediately analyzed by flow cytometry. For CLSM imaging, cells were seeded onto the coverslips, and then treated as mentioned above. Finally, cells were fixed with 4% paraformaldehyde and stained with DAPI for CLSM observation.

To evaluate the extracellular ATP level, B16F10 cells and 4T1 cells were treated with above drugs for 24 h. The medium was collected and centrifugated to remove cell debris. The supernatant was detected according to luciferase-based ATP assay kit (Beyotime, Shanghai, China).

The intracellular HMGB1 and extracellular HMGB1 and TFAM protein level were detected by Western blot. Briefly, B16F10 cells were treated with above drugs for 24 h, and then both medium and cells were collected. After SDS-PAGE separation, the HMGB1 and TFAM proteins were transferred to polyvinylidene fluoride membranes and incubated with primary antibodies at 4 °C overnight, followed by HRP-labelled goat anti-rabbit secondary antibodies incubation at 37 °C for 2 h. Actin was used as the control protein. The chemiluminescence was evaluated on a Bio-Rad ChemiDoc XRS System (BioRad, CA, USA).

2.9. Evaluation of phagocytosis and maturation of bone marrow-derived dendritic cells

For quantitative analysis, B16F10 cells were first labelled with cell-tracker CMFDA (5 μmol/L) for 30 min, and then treated with P-D-R8MTS, P-MSP-DMA (pH 7.4 and 6.5) and SNV (pH 7.4 and 6.5) for 24 h. Bone marrow-derived dendritic cells (BMDCs) were extracted from the bone marrow of C57BL/6 mice, and then stained with anti-CD11C-APC (1:333) at 4 °C for 1 h. After that, B16 cells and BMDCs were mixed (1:1) and incubated for 2 h (37 °C, 50 rpm) and immediately analyzed by flow cytometry. For CLSM analysis, B16F10 cells were first treated with drugs for 24 h, and then collected and stained with DiR (2 μg/mL, 37 °C) for 1.5 h. BMDCs were seeded on coverslips, and then labelled with CMFDA for 1h. After that, B16 cells were mixed with BMDCs and incubated for 2 h (37 °C). Cells were fixed and stained with DAPI CLSM observation.

To investigate the maturation of DCs after uptaking tumor antigens, B16F10 cells (1×10^5 cells/well) were seeded onto 12-well plates and treated with P-D-R8MTS, P-MSP-DMA (pH 7.4 and 6.5) and SNV (pH 7.4 and 6.5) for 24 h. Then B16F10 cells were collected and incubated with BMDCs for another 24 h. Cells were collected and blocked with 5% goat serum for 20 min, and then stained with anti-CD11C-FITC (1:200), anti-CD80-APC (1:200) and anti-CD86-PerCP/Cy5.5 (1:200) at 4 °C for 1 h. After that, cells were washed and analyzed by flow cytometry.

2.10. Evaluation of PD-L1 level

B16F10 cells and 4T1 cells were treated with MSP, P-D-R8MTS, P-MSP-DMA (pH 7.4 and 6.5) and SNV (pH 7.4 and 6.5) for 24 h. After that, cells were blocked with 5% goat serum for 20 min, and then incubated with anti-CD274-APC antibody (1:200 dilution) at 4 °C for 1 h. Cells were washed and immediately analyzed by flow cytometry.

2.11. Apoptosis and cytotoxicity assays

APC Annexin V Apoptosis Detection Kit with 7-aminoactinomycin D (7-AAD) (Biolegend, San Diego, CA, USA) was used to evaluate apoptosis level according to the manufacturer's protocols. Briefly, B16F10 cells were incubated with P-D-R8MTS, P-MSP-DMA (pH 7.4 and 6.5) and SNV (pH 7.4 and 6.5) for 24 h. Cells were collected and washed twice with PBS. The pellets of cells were resuspended in 100 μL binding buffer and then added into 5 μL APC Annexi*n*-V and 5 μL 7-AAD followed by 15 min incubation at room temperature. Afterwards, binding buffer (400 μL) was added and samples were monitored by flow cytometry immediately.

For cytotoxicity assessment, MTT assay was used. B16F10 cells were seeded onto 96-well plates and treated with copolymers and SNV at pH 7.4 or pH 6.5 for 24 and 48 h. Then 20 μL MTT solution (5 mg/mL) was added and cultured for 4 h. The medium was removed and 150 μL dimethyl sulfoxide (DMSO) was added to dissolve the formazan. The absorbance at 570 nm was detected with microplate reader (Bio-Rad, Microplate Reader 550, CA, USA) and cell viability and IC_{50} value were calculated.

2.12. Pharmacokinetics and biodistribution in vivo

BALB/c mice were randomly divided into 3 groups ($n = 5$), and intravenously injected with free DOX, P-D-R8MTS and SNV with an equivalent DOX dose of 5 mg/kg. At predetermined time points (0, 0.08, 0.25, 0.5, 1, 2, 3, 4, 8, 12, and 24 h), 40 μL of whole blood was collected from the orbita and extracted by acetone to detect DOX concentration in blood.

To investigate the *in vivo* biodistribution, B16F10 cells (4×10^5 cells) and 4T1 cells (3×10^4 cells) were subcutaneously injected into the right flank of C57BL/6 female mice and the third mammary fat pad of BALB/c female mice, respectively. When

tumors grew to 200−300 mm^3, mice were intravenously injected with Cy5, Cy5-labeled P-D-R8MTS (P-D-R8MTS-Cy5) and Cy5-labeled SNV (P-D-R8MTS-Cy5 assembled with P-MSP-DMA) with an equivalent Cy5 dose of 5 nmol/L. At predetermined time points (1, 6, 12, and 24 h after administration), living imaging of the whole body and excised organs (24 h after administration) was captured using the IVIS optical imaging system.

To investigate the pH-sensitive behavior of SNV in tumors, B16F10 cells (4×10^5) were subcutaneously injected into the right flank of C57BL/6 female mice. When tumors grew to 200−300 mm^3, mice were intravenously injected with SNV (P-D-R8MTS-Cy5 assembled with P-MSP-DMA-Cy3) with an equivalent Cy5 dose of 5 nmol/L. At predetermined time points (1, 4, and 8 h post-injection), mice were sacrificed and tumors were frozen at −40 °C overnight. Then tumors were cut into 10 μm-slices. Afterwards, the sections were washed, fixed with 4% paraformaldehyde and stained with DAPI (5 μg/mL) for 4 min. The fluorescence images were analyzed by confocal laser scanning microscopy.

To further investigate the *in vivo* mitochondrial targeting efficacy, B16F10 tumor-bearing mice were established as mentioned above. When tumors grew to 200−300 mm^3, mice were intravenously injected with free DOX, P-D-R8MTS and SNV (equivalent DOX dose 5 mg/kg) as well as negative saline. After 12 h administration, mice were sacrificed and tumors were taken out. A part of tumors was homogenized and filtered through a 70 μm nylon mesh filters, and incubated with ACK lysing buffer (4 °C, 10 min) to obtain single cell suspensions. Cells were stained with anti-CD45-PerCP/Cy5.5 at 4 °C for 1 h and washed twice. The rest of tumors were used to isolate mitochondria according to Tissue Mitochondria Isolation Kit protocols. All the steps were performed on ice. The cells and mitochondria were suspended and analyzed by flow cytometry immediately.

2.13. Investigation of antitumor and immune responses in B16F10 tumors

B16F10 cells (4×10^5 cells) were subcutaneously injected into the right flank of C57BL/6 female mice on day 0. When tumor volume reached 100 cm^3 on Day 8, mice were intravenously injected with saline, free DOX, P-MSP-DMA, P-D-R8MTS and SNV with an equivalence DOX dose of 5 mg/kg and equivalence MSP dose of 5 mg/kg on Days 8, 11 and 14. On Day 19, mice were sacrificed, and tumors were harvested and homogenized to single cell suspensions as the same method mentioned above. To evaluate ICD induction, cells were stained with anti-CD45-PerCP/Cy5.5 (1:200) and anti-CRT-antibodies (1:500 dilution) at 4 °C for 1 h. Then, cells were washed and stained with Alexa Fluor 647-conjugated second antibody (1:500 dilution) for 45 min. Afterwards, cells were washed and analyzed by flow cytometry. For the analysis of mature dendritic cells (DCs) in tumor, cells were stained with anti-CD11C-FITC (1:200),anti-CD80-APC (1:200) and anti-CD86-PE (1:200) at 4 °C for 1 h, and then cells were washed and analyzed by flow cytometry. To measure immune cells including cytotoxic T lymphocytes (CTLs, $CD3^+CD4^-CD8^+$), T effector cells (Teff, $CD3^+CD4^+CD8^-$), regulatory T cells (Tregs, $CD3^+CD4^+Foxp3^+$) in tumors, cells were incubated with anti-CD16/32 antibody at 4 °C for 20 min, and then stained with anti-CD3-FITC (1:300), anti-CD8-APC (1:300), anti-CD4-PerCP/Cy5.5 (1:200), anti-FOXP3-PE (1:200) at 4 °C for 1 h. Afterwards, cells were washed and analyzed by flow cytometry. For evaluation of PD-L1 expression in tumors, cells were stained with anti-CD45-PerCP/Cy5.5 (1:200) and anti-CD274-APC antibodies (1:200) at 4 °C for 1 h. Then cells were washed for flow cytometry analysis. To determine the secretion of mitochondrial transcription factor A (TFAM), interferon γ (IF*N*-γ) and expression of inflammatory cytokines IL-6, CHOP, GRP78 and P-ELF2α, tumors were harvested and embedded in paraffin. Then tumors were cut into 10 μm-slices. Afterwards, the sections were washed, fixed with 4% paraformaldehyde and stained with anti-CHOP antibody (1:500 dilution), anti-GPR78 antibody (1:100 dilution) and anti- P-ELF2α antibody (1:100 dilution) at 4 °C overnight, and Cy3-conjugated second antibody (1:500 dilution) at room temperature for 45 min. The sections were washed and stained with DAPI (5 μg/mL) for 4 min. The fluorescence images were analyzed by confocal laser scanning microscopy. For safety evaluation, major organs were collected and fixed with 4% paraformaldehyde, followed by paraffin embedding and H&E (hematoxylin and eosin) staining.

For CD8-depletion assay, B16F10 tumor-bearing mice were established as mentioned above. When tumors grew to 100 cm^3 on Day 8, mice were intravenously injected with saline and SNV with or without CD8-delepting antibody at an equivalence DOX dose of 5 mg/kg on Days 8, 11 and 14. The tumor volume and survival rate were monitored.

2.14. Antitumor and anti-metastasis efficacy in 4T1 tumors

To evaluate immune responses in poorly immunogenic 4T1 tumor, 4T1 cells (3×10^4 cells) were injected into the third mammary fat pad of BALB/c female mice on Day 0. When tumor volume reached 100 cm^3 on Day 7, mice were intravenously injected with saline, free DOX, P-MSP-DMA, P-D-R8MTS and SNV with an equivalence DOX dose of 3.5 mg/kg and equivalence MSP dose of 3.5 mg/kg on Days 7 and 10. On Day 11, tumors were harvested, and the induction of ICD and immune cells were measured as the same method mentioned above. To assess the therapeutic efficacy, 4T1 tumor-bearing mice were intravenously injected with saline, free DOX, P-MSP-DMA, P-D-R8MTS and SNV every 3 day for 4 rounds. The tumor volume was monitored. On Day 24, mice were sacrificed, and tumors were harvested. For lung metastasis evaluation, lungs were fixed with Bouin's solutions for 4 h and then the white metastatic nodules were counted. For analysis of $CD8^+$ T cells and PD-L1 expression, lungs were embedded in paraffin. Then lungs were cut into 10 μm-slices. Afterwards, the sections were washed, fixed with 4% paraformaldehyde and stained with anti-CD8 (1:100) and anti-PD-L1 (1:100) at 4 °C overnight, and Cy3-conjugated second antibody (1:100 dilution) at room temperature for 45 min. The sections were washed and stained with DAPI (5 μg/mL) for 4 min. The fluorescence images were analyzed by confocal laser scanning microscopy. Other major organs were collected and stained with H&E for safety analysis.

2.15. Statistical analysis

Statistical analysis was calculated by one-way ANOVA analysis among multiple groups followed by Tukey's multiple comparison using SPSS 22.0 software. P value <0.05 was recognized as statistically significant.

3. Results and discussion

3.1. *P-D-R8MTS triggers enhanced immunogenic cell death*

As previously reported, *N*-(2-hydroxypropyl) methacrylamide (HPMA) copolymer-doxorubicin conjugate (PD) containing pH-sensitive hydrazone linkage was firstly synthesized through radical solution copolymerization, and then decorated with cell penetrating peptide R8 and mitochondrial targeted hybrid peptide R8MTS *via* click chemistry to obtain P-D-R8 and P-D-R8MTS (Supporting Information Fig. S1A)[14]. As displayed in ^{1}H NMR spectrum (Fig. S1B), P-D-R8MTS showed the characteristic peak of protons in HPMA around 4.7 ppm, the aromatic protons in DOX around 7.2 ppm and the characteristic peak of R8MTS peptide around 4.0−4.5 ppm and 7.0−8.5 ppm. Their characterizations including molecular weight, zeta potential, drug loading and peptide content were displayed in Fig. 1A. Each copolymer possessed similar cationic charge and doxorubicin (DOX) loading.

Firstly, we investigated their cell internalization and intracellular distribution in melanoma B16F10 cells. As shown in Fig. 1B–D, both P-D-R8 and P-D-R8MTS could significantly increase the cellular uptake of HPMA copolymer-doxorubicin conjugate (Fig. 1B), while only P-D-R8MTS augmented mitochondrial accumulation (3.2- and 2.34-fold higher than PD and P-D-R8, respectively, Fig. 1C and D), suggesting R8MTS modification favored effective mitochondrial targeting. As a result of abundant mitochondrial distribution, P-D-R8MTS exhibited the highest intracellular reactive oxygen species (ROS) level (3.36-and 2.20-fold higher than control and PD, respectively, Fig. 1E). Interestingly, we found that compared with non-targeted PD, mitochondrial-targeted P-D-R8MTS considerably facilitated the surface exposure of calreticulin (CRT, Fig. 1F), extracellular release of adenosine triphosphate (ATP, Fig. 1G) and high mobility group protein B1 (HMGB1, Fig. 4C), demonstrating P-D-R8MTS was more capable to provoke immunogenic cell death (ICD). As compared with P-D-R8MTS, although P-D-R8 had comparable cellular uptake, its capacity of ICD induction was much weaker. This revealed the enhanced ICD was largely ascribed to mitochondrial targeting and ROS generation of P-D-R8MTS rather than the increased cell internalization.

We further investigated the underlying mechanism. Previous studies have shown that ROS originating from mitochondria could disrupt the ER homeostasis to induce ER stress, leading to CRT translocation from ER to cell surface and ICD induction[23−25]. Therefore, we evaluated whether P-D-R8MTS could trigger ER

A

Copolymer characterization	Molecular weight (kDa)	PDI	Zeta potential (mV)	Drug loading (wt %)	Peptide (μmol/g)
PD	20.60	1.08	19.20 ± 1.80	7.10	–
P-D-R8	22.60	1.24	19.70 ± 0.82	7.53	57
P-D-R8MTS	27.90	1.15	28.97±1.15	6.65	62

PDI, polydispersity index; –, not applicable. Data are presented as mean±SD (*n*=3).

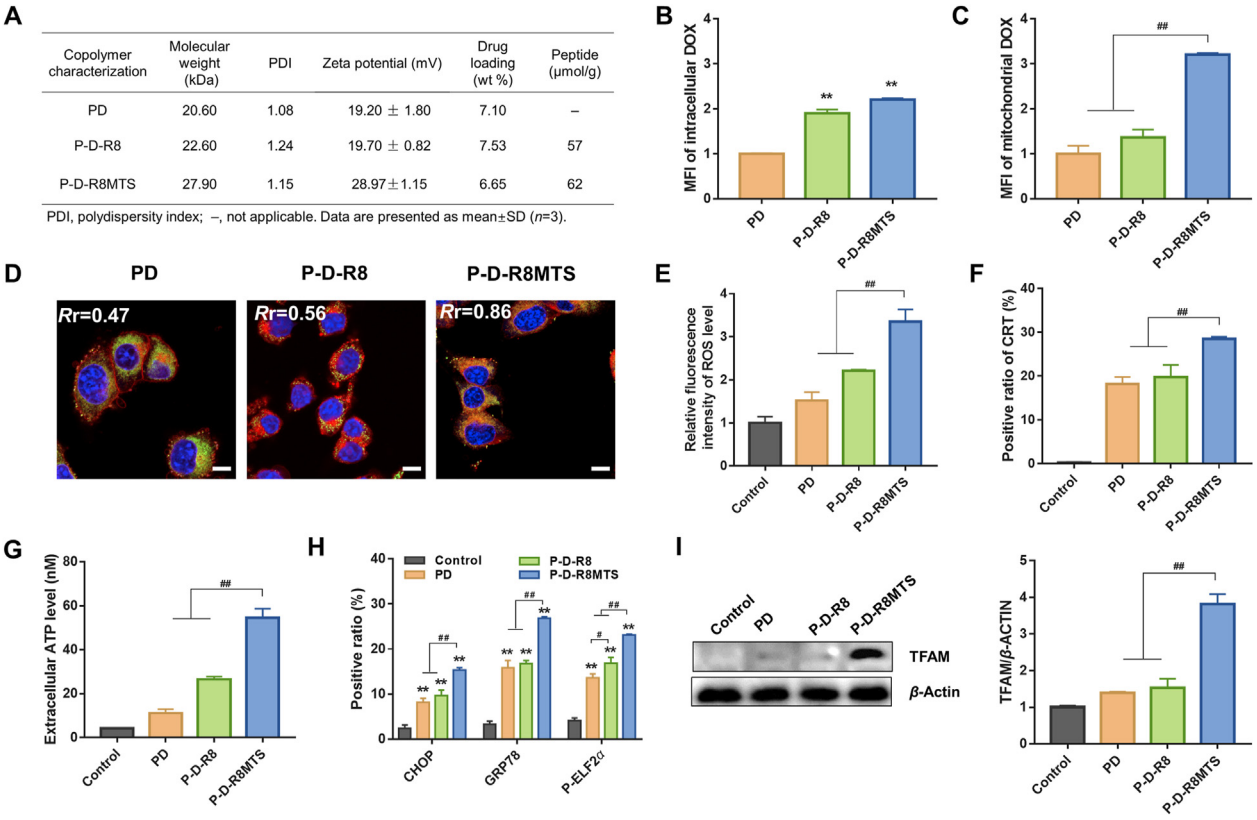

Figure 1 (A) Characterization of the HPMA copolymer-DOX conjugates. (B) Cellular uptake of B16F10 cells for 4 h by flow cytometry. (C) Analysis of mitochondrial accumulation on B16F10 cells for 4 h by CLSM and (D) flow cytometry. Blue: nucleus; Green: mitochondria; Red: DOX, Rr: Pearson correlation coefficient. Higher Rr indicates better colocalization between fluorophores. Scale bar: 10 μm. (E) ROS level of B16F10 cells after treated with PD, P-D-R8 and P-D-R8MTS for 12 h. (F) Ecto-calreticulin and (G) extracellular ATP level of B16F10 cells after treated with PD, P-D-R8 and P-D-R8MTS for 24 h. ** indicated $P < 0.01$ *versus* PD. ## indicated $P < 0.01$. (H) Expression of CHOP, GRP78 and P-ELF2α on B16F10 cells treated with PD, P-D-R8 and P-D-R8MTS for 24 h. (I) TFAM expression and quantification in the extracellular supernatant by western blot. Results were mean ± SD ($n = 3$). ** indicated $P < 0.01$ *versus* Control group. # and ## indicated $P < 0.05$ and $P < 0.01$, respectively. The equivalent DOX concentration was 10 μg/mL.

stress. We measured three typical ER stress-mediated marker proteins: C/EBP homologous protein (CHOP), glucose-regulated protein 78 (GRP78) and phosphorylated eukaryotic translation initiation factor2α (P-ELF2α). Results in Fig. 1H demonstrated that P-D-R8MTS induced much higher expression of these marker proteins than PD and P-D-R8. Moreover, in addition to ROS and ATP, damaged mitochondria could also secrete other mitochondria-associated damage molecules[12,26]. Mitochondrial transcription factor A (TFAM), a mitochondrial DNA-binding protein, can convey danger signal upon cell death by binding to advanced glycosylation end product-specific receptor (AGER) on plasmacytoid dendritic cells to induce inflammatory response, which was structurally and functionally homologous to HMGB1. A recent study reported that extracellular release of TFAM contributed to ICD induction[11]. Thus, we investigated whether the increased ROS generation by P-D-R8MTS could promote TFAM release. As expected, the Western blot analysis showed that P-D-R8MTS considerably facilitated extracellular release of TFAM on B16F10 cells, whereas PD and P-D-R8 exhibited fairly low TFAM expression (Fig. 1I). Taken together, by targeting mitochondria to induce substantial ROS generation, P-D-R8MTS was capable of not only triggering ER stress, but also promoting secretion of mitochondria-associated damage molecules, which amplified ICD efficacy.

3.2. Preparation, characterization and PD-L1 downregulation of self-assembled nano vehicle (SNV)

Of note, we found that after P-D-R8MTS treatment, the expression of PD-L1 was increased in B16F10 cells (Fig. 2A and B), which was corresponding to previous studies that chemotherapeutics could adaptively upregulate PD-L1 to aggravate immunosuppressive environment and offset efficacy of ICD[16,27]. Therefore, simultaneously enhancing immune-stimulation and relieving immunosuppression is crucial for efficient immunotherapy.

Here, we constructed a multifunctional self-assembled nano vehicle (SNV) combining ICD induction and anti-PD-L1. PD-L1 antagonistic peptide MSP, reported to possess high affinity to bind PD-L1, was grafted on HPMA copolymers by click chemistry and then modified with dimethylmaleic anhydride (DMA) to obtain P-MSP-DMA (Supporting Information Fig. S2 and Fig. S3A)[28]. As displayed in ^{1}H NMR spectrum (Fig. S2B), P-MSP-DMA showed the characteristic peak of protons in HPMA around 4.7 ppm, the methyl protons in DMA around 2.9 ppm and the characteristic peak of MSP peptide around 6.5−8.5 ppm, indicating the successful synthesis of P-MSP-DMA. The cationic P-D-R8MTS (+28.97 mV) was then self-assembled with anionic P-MSP-DMA (−21.46 mV) *via*

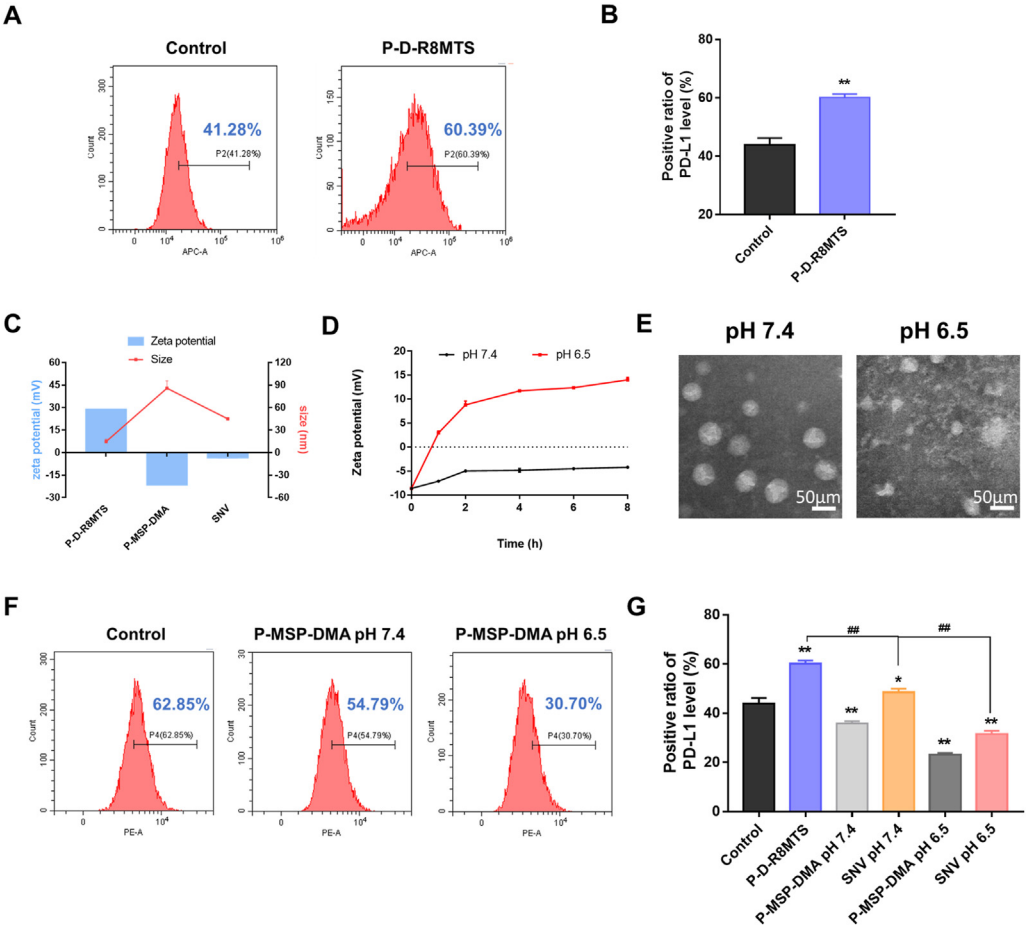

Figure 2 (A, B) PD-L1 level of B16F10 cells after treated with P-D-R8MTS for 24 h. (C) Size and zeta potential of copolymers and SNV. (D) Zeta potential variation of P-MSP-DMA as a function of incubation time at pH 7.4 or 6.5. (E) Transmission electron images of SNV incubated at pH 7.4 or 6.5 for 2 h. Scale bar: 50 nm. (F, G) PD-L1 level of B16F10 cells after treated with various copolymers and SNV for 24 h. Results were mean ± SD (n = 3). * and ** indicated $P < 0.05$ and $P < 0.01$ *versus* control group, respectively. $^{\#\#}$ indicated $P < 0.01$.

electrostatic interaction to form SNV. The dynamic light scattering showed the size of SNV was ~45 nm with a mildly negative charge (−3.49 mV), indicating the successful assembly of SNV (Fig. 2C). After incubation in PBS containing 50% serum for 24 h, no obvious particle size and zeta potential change were observed in SNV, suggesting SNV remained good serum stability (Fig. S3B and S3C). Next, we evaluated the charge reversal capacity of P-MSP-DMA (Fig. 2D). In PBS (pH 7.4), the zeta potential of P-MSP-DMA remained relatively stable over 8 h, while it reversed quickly from negative to positive charge within 2 h in PBS (pH 6.5). This demonstrated P-MSP-DMA possessed pH responsive charge reversal, which could sequentially lead to disintegration of SNV in acidic tumor microenvironment. Transmission electron microscopy (TEM) images also showed at pH 7.4, the morphology of SNV was compact and spherical, whereas it converted to irregular loose structure at pH 6.5, confirming the disassembly of SNV in acidic condition (Fig. 2E). Besides, *in vitro* drug release profile displayed that DOX release of P-D-R8MTS and SNV at pH 7.4 were relatively low (~20%) over 48 h incubation, but significantly augmented at pH 6.5 and pH 5.0 (Fig. S3D), indicating that both copolymers and SNV exhibited pH-dependent drug release.

Next, we investigated the anti-PD-L1 efficiency of P-MSP-DMA on B16F10 cells. As presented in Fig. 2F and Supporting Information Fig. S4, MSP peptide exhibited significant down-regulation of PD-L1. P-MSP-DMA slightly declined PD-L1 expression at pH 7.4, while at pH 6.5, the PD-L1 level was decreased sharply. It was because after DMA detachment from HPMA copolymer at pH 6.5, P-MSP possessed higher affinity with cell membrane *via* electrostatic interaction, thus facilitating the binding of P-MSP with PD-L1. These results demonstrated that P-MSP-DMA was capable of reducing surface PD-L1 on B16F10 cells and conjugating MSP to HPMA copolymer would not affect the PD-L1 binding and blocking efficacy of MSP. Therewith, we further investigated whether P-MSP-DMA could reverse the upregulation of PD-L1 caused by P-D-R8MTS (Fig. 2G). Compared with control group, P-D-R8MTS remarkably increased the expression of PD-L1. However, after SNV treatment, the surface PD-L1 of B16F10 cells was conspicuously descended both at pH 7.4 and 6.5. Particularly, the PD-L1 expression of SNV (pH 6.5)-treated group was 71.9% of control group and 52.5% of P-D-R8MTS group. As a result, P-MSP was able to reverse the upregulation of PD-L1 induced by DOX, thus mitigating immunosuppression.

3.3. *SNV targets tumor mitochondria and triggers apoptosis*

To evaluate cellular behaviors of SNV, we investigated its internalization in B16F10 cells at first. As displayed in Supporting Information Fig. S5A, both P-D-R8MTS and SNV were time-dependent cell internalization. As expected, the uptake of SNV at pH 7.4 was significantly lower than that of P-D-R8MTS, which might be attributed to charge shielding of R8 by P-MSP-DMA.

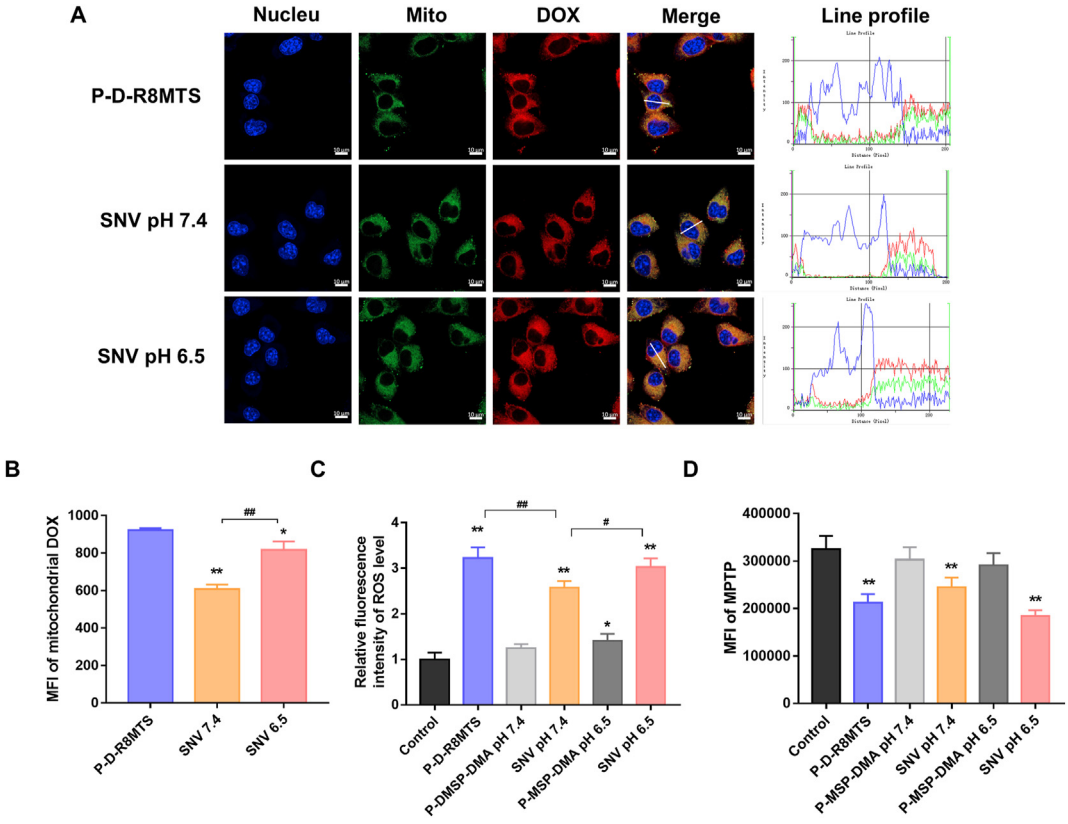

Figure 3 (A) Qualitative (by CLSM) and (B) quantitative (by flow cytometry) analysis of DOX accumulation in mitochondria of B16F10 cells for 4 h. Blue: nucleus; Green: mitochondria; Red: Dox. Scale bar: 10 μm. Results were mean ± SD ($n = 3$). * and ** indicated $P < 0.05$ and $P < 0.01$ *versus* P-D-R8MTS group, respectively. ## indicated $P < 0.01$. (C) ROS level and (D) MPTP opening of B16F10 cells after treated with copolymers and SNV. Results were mean ± SD ($n = 3$). * and ** indicated $P < 0.05$ and $P < 0.01$ *versus* control group, respectively. # and ## indicated $P < 0.05$ and $P < 0.01$, respectively.

When pH was at 6.5, the uptake of SNV recovered, indicating disintegration of SNV and exposure of R8. Then we investigated the uptake mechanism of P-D-R8MTS and SNV (Fig. S5B). The results demonstrated that P-D-R8MTS entered into B16F10 cells *via* energy-dependent clathrin-mediated endocytosis and macropinocytosis, while SNV at pH 7.4 was through clathrin- and caveolae-mediated endocytosis. It was because that R8 modification would mediate macropinocytosis[29,30]. When R8 was shielded, SNV bypassed macropinocytosis and entered cells by other means. As pH decreased to 6.5, SNV showed the same endocytosis mechanism as P-D-R8MTS, suggesting the disassembly of SNV in acidic tumor microenvironment. Furthermore, we investigated whether SNV could disassemble at pH 6.5 by CLSM. P-MSP-DMA was labelled with Cyanine5 (Cy5) and self-assembled with P-D-R8MTS. As displayed in Supporting Information Fig. S6, for 1h, most of SNV remained integrated with overlapping of green and red channel, resulting in bright yellow fluorescence. After 4 h incubation, the cellular uptake of SNV increased and the green and red fluorescence was separated. P-D-R8MTS distributed in cytoplasm, whereas P-MSP-DMA-Cy5 mainly bound with cytomembrane. These results further confirmed that SNV was able to disassemble at pH 6.5 and release both copolymers.

Next, we investigated whether SNV could also target mitochondria. Results from CLSM and flow cytometry showed that SNV was capable of delivering DOX to mitochondria at pH 7.4 and 6.5 (Fig. 3A and B). The mitochondrial targeting efficiency of SNV at pH 7.4 was slightly inferior than that of pH 6.5, possibly because P-MSP-DMA hindered the cellular uptake of P-D-R8MTS. After that, we assessed the effect of SNV on mitochondrial function. As expected, SNV could

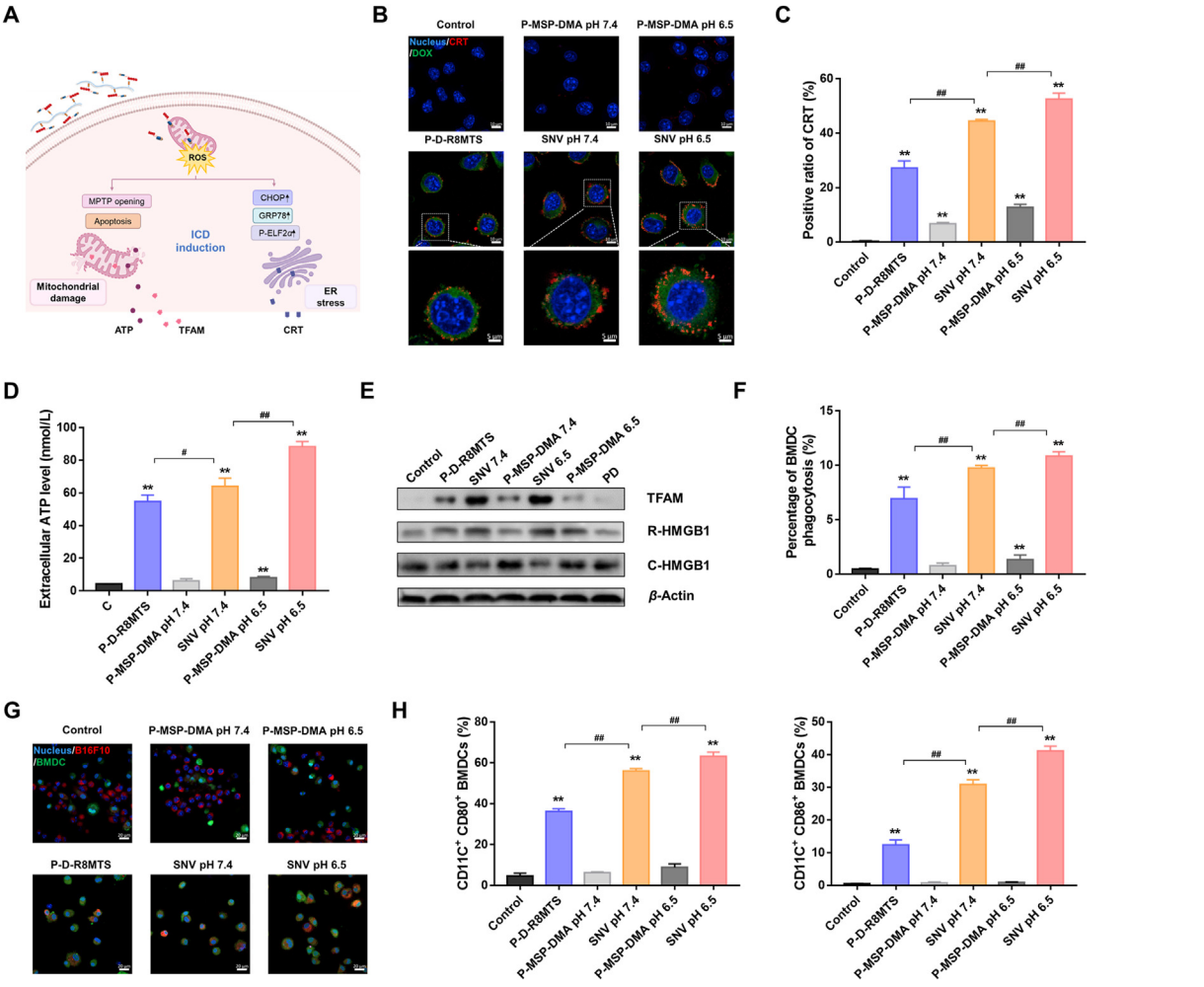

Figure 4 (A) Illustration of ICD induction by P-D-R8MTS. P-D-R8MTS targeted mitochondria to promote substantial ROS generation. On one aspect, ROS induced apoptosis to promote release of mitochondria-associated damage molecules (TFAM and ATP). On another aspect, ROS triggered ER stress with elevated expression of marker proteins (CHOP, GRP78 and P-ELF2α), leading to surface exposure of CRT. As a consequence, P-D-R8MTS induced massive ICD. (B, C) Ecto-calreticulin expression of B16F10 cells analyzed by CLSM and flow cytometry. Blue: nucleus; Green: DOX; Red: ecto-CRT. (D) Extracellular ATP level of B16F10 cells treated with copolymers and SNV for 24 h. (E) TFAM expression in the extracellular supernatant, HMGB1 expression in whole cell lysate (C-HMGB1) and in the extracellular supernatant (R-HMGB1). (F, G) Percentage of BMDC phagocytosis towards B16F10 cells pre-treated with copolymers and SNV for 24 h. Data were analyzed by flow cytometry and CLSM. Blue: nucleus; Green: BMDCs; Red: B16F10 cells. Scale bar: 20 μm. (H) BMDCs maturation after phagocytosis of B16F10 cells treated with copolymers and SNV for 24 h. Results were mean ± SD ($n = 3$). ** indicated $P < 0.01$ *versus* control group. $^{\#}$ and $^{\#\#}$ indicated $P < 0.05$ and $P < 0.01$, respectively.

cause apparent mitochondrial damage, leading to considerably elevated ROS level (Fig. 3C) and mitochondrial permeability transition pores (MPTPs) opening (Fig. 3D). Collectively, SNV could efficiently deliver DOX to mitochondria and induce mitochondrial dysfunction.

Having confirmed mitochondria-targeted disorders of SNV, we further investigated its impact on cell apoptosis. Supporting Information Fig. S7A showed that P-D-R8MTS gave rise to 67.34% early apoptosis after 24 h incubation with B16F10 cells. Owing to the participation of PD-L1 in anti-apoptotic pathways (*e.g.*, AKT/mTOR signaling), P-MSP-DMA triggered mild apoptosis, which resulted in stronger early apoptosis of SNV at pH 7.4 than P-D-R8MTS[31−33]. When at pH 6.5, P-MSP significantly decreased PD-L1 level to induce higher apoptosis, leading to further late apoptosis (28.68%) proceeding of SNV. The cytotoxicity result was consistent with cell apoptosis (Fig. S7B). P-MSP-DMA alone was low toxic, but after self-assembled with P-D-R8MTS, it could significantly enhance cytotoxicity of SNV (Supporting Information Table S1). Taken together, SNV was able to target mitochondria to bring about intense cell apoptosis and anticancer proliferation efficacy *in vitro*.

3.4. *SNV enhances immunogenic cell death*

Having demonstrated P-D-R8MTS induced ICD, we next investigated the efficacy of SNV on B16F10 cells by evaluating the release of DAMPs. Due to its inferior ROS generation and apoptosis initiation, the surface CRT exposure of P-MSP-DMA was relatively low (Fig. 4B and C). Interestingly, compared with P-D-R8MTS (27.13%), SNV triggered significantly higher CRT expression both at pH 7.4 (44.45%) and pH 6.5 (52.58%). CLSM imaging was coincident with quantitative analysis, SNV-treated

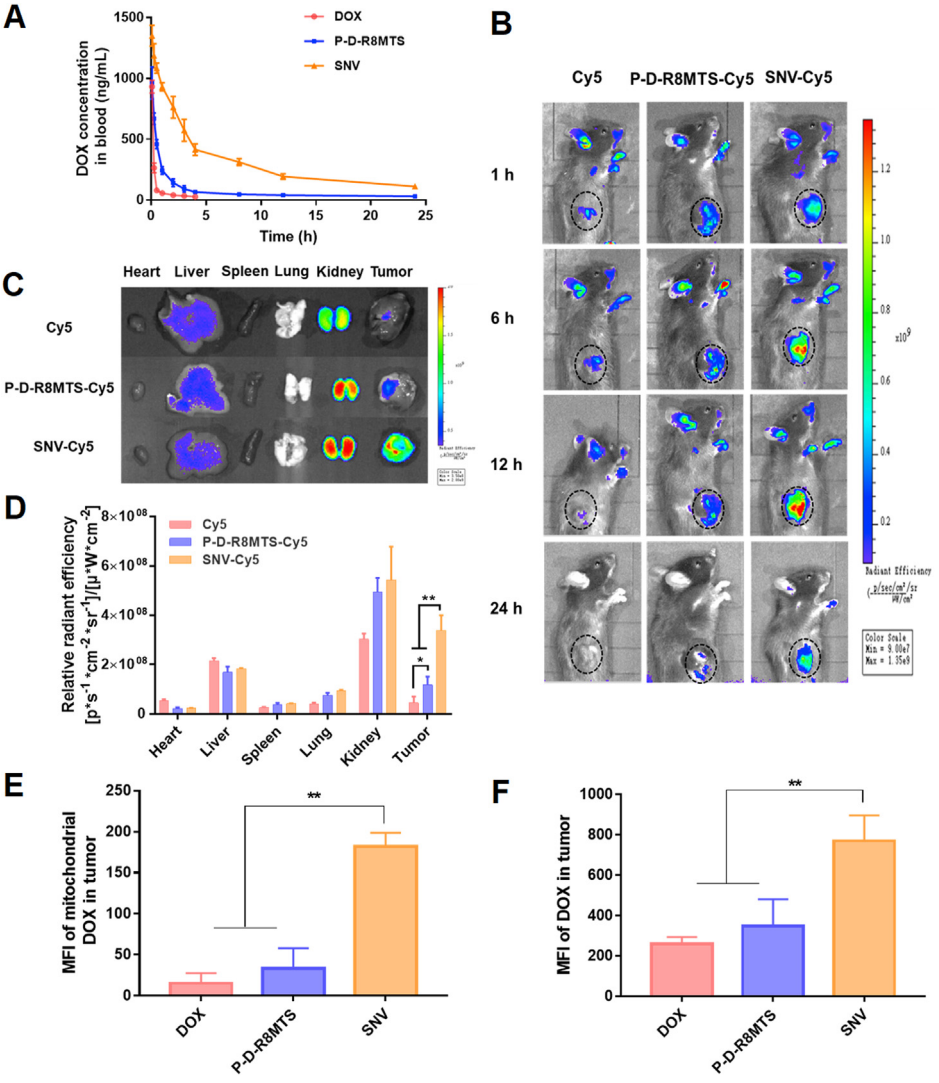

Figure 5 (A) Pharmacokinetics of free DOX, P-D-R8MTS and SNV after intravenous injection. At different time points, blood samples were taken and the concentration of DOX in blood was analyzed. Results were mean ± SD ($n = 5$). (B) Representative *in vivo* images of B16F10 tumors in C57/BL6 mice at 1, 6, 12 and 24 h post-injection of Cy5-labeled HPMA copolymers or SNV. (C) Representative *ex vivo* images and (D) corresponding semi-quantitative radiant efficiency of main organs from B16F10 tumor-bearing C57/BL6 mice at 24 h post-injection of Cy5-labeled HPMA copolymers or SNV. Accumulation of DOX in (E) tumor tissue and in (F) tumor mitochondria after intravenous injection of free DOX, P-D-R8MTS and SNV for 12 h. Results were mean ± SD ($n = 3$). * and ** indicated $P < 0.05$ and $P < 0.01$, respectively.

cell surface exhibited brighter red dot fluorescence of CRT than P-MSP-DMA and P-D-R8MTS. It was because that SNV elicited stronger apoptosis, leading to more disruption of ER homeostasis[23–25]. Analysis of ER stress also confirmed that SNV triggered the highest expression of CHOP, GRP78 and P-ELF2α, suggesting intensive ER stress caused by SNV (Supporting Information Fig. S8). Then we evaluated the extracellular ATP level, a well-known "find me" signal for dendritic cells (DCs) recognition. Consistent to CRT trend, SNV (pH 6.5) brought about the highest ATP release (Fig. 4D). Besides, Western blot results indicated SNV slightly decreased cellular HMGB1 level of B16F10 cells, and remarkably upregulate extracellular HMGB1 expression (Fig. 4E, and Fig. S8). Moreover, SNV could considerably facilitate TFAM release compared to P-D-R8MTS and P-MSP-DMA, of which SNV (pH 6.5) possessed the strongest ability to trigger extracellular TFAM release owing to the highest apoptosis (Fig. 4E, Fig. S8). Collectively, SNV significantly strengthened ICD efficacy by inducing massive apoptosis and ER stress (Fig. 4A).

As reported, tumor cell-surface CRT, characterized as an "eat me" signal, could facilitate engulfment by APCs such as DCs. Then HMGB1 and TFAM act as "danger" signal to bind to DCs, promoting antigen presentation to T cells[3]. Therefore, we further investigated whether these DAMPs would motivate phagocytosis of B16F10 cells by bone marrow-derived dendritic cells (BMDCs) *in vitro*. B16F10 cells were pretreated with different copolymers or SNV, and then incubated with BMDCs for 2 h. As displayed in Fig. 4F and G, P-MSP-DMA failed to promote BMDCs phagocytosis, whereas cells treated with SNV exhibited significant phagocytosis by BMDCs. Besides, images from CLSM showed that the engulfment of control and P-MSP-DMA group was relatively weak, presenting obviously separated red (B16F10 cells) and green (BMDCs) fluorescence. In contrast, cells treated with P-D-R8MTS exerted mild overlap of red and green fluorescence, implying portion of B16F10 cells were phagocytosed by BMDCs. Particularly, SNV (pH 6.5) group exhibited the strongest orange-yellow fluorescence, which indicated SNV prominently triggered engulfment of B16F10 cells by BMDCs. After that, the BMDCs maturation was evaluated (Fig. 4H). P-D-R8MTS significantly promoted maturation of BMDCs after B16F10 cells phagocytosis, while P-MSP-DMA had nearly no effect on BMDCs maturation. As expected, SNV exhibited the highest promotion efficacy on BMDCs maturation, demonstrating that SNV was able to motivate BMDCs maturation after phagocytosis of B16F10 cells. To sum up, SNV was able to amplify ICD of cancer cells and promote immune recognition and response.

3.5. *Antitumor and immune responses of SNV in vivo*

Having indicated the efficient ICD induction of SNV *in vitro*, we wondered whether it could translate to augmented antitumor efficacy *in vivo*. Firstly, we evaluated the pharmacokinetics of SNV. As displayed in Fig. 5A and Supporting Information Table S2, SNV significantly prolonged the blood circulation of DOX (with enhanced AUC and $t_{1/2}$) compared with free DOX and cationic P-D-R8MTS. After that, we labeled P-D-R8MTS with near-infrared fluorescent Cy5 to investigate the biodistribution of P-D-R8MTS and SNV in B16F10 tumor-bearing C57/BL6 mice. Images showed that both free Cy5 and cationic P-D-R8MTS-Cy5 exhibited insufficient tumor accumulation and rapid clearance (Fig. 5B). In contrast, much stronger fluorescence was observed in tumors from SNV-Cy5-treated mice at each time point. Particularly, *ex vivo* semi-quantitative analysis at 24 h demonstrated the

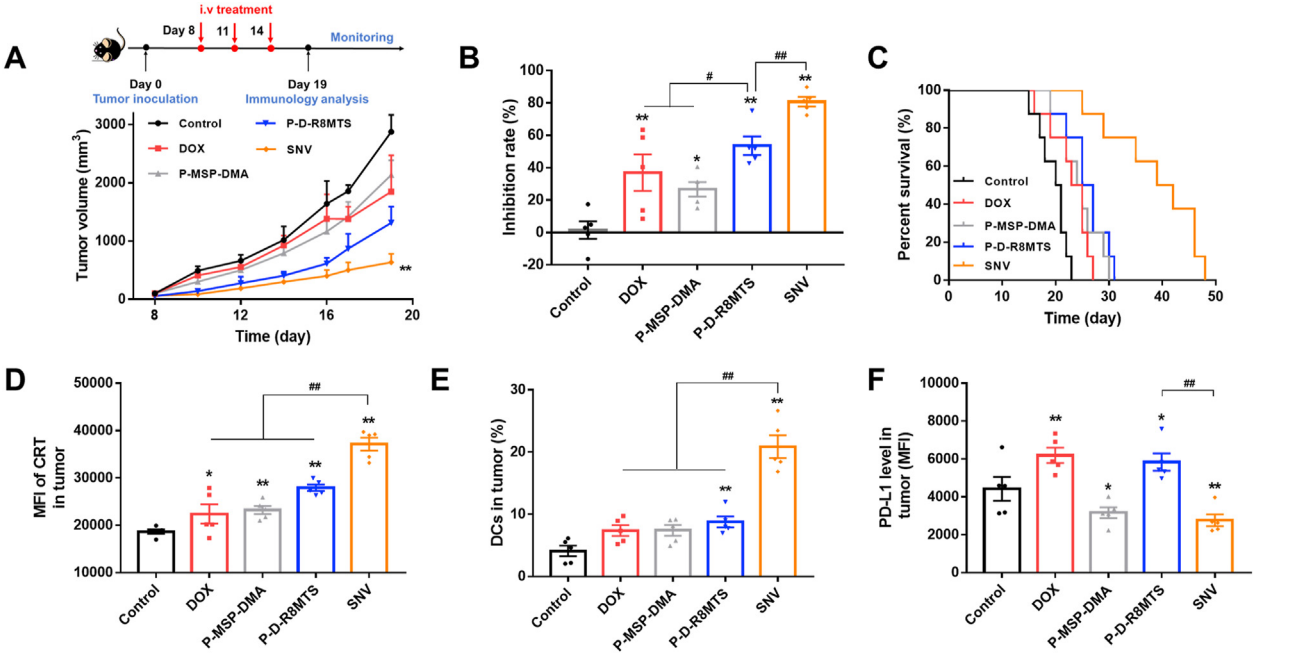

Figure 6 *In vivo* antitumor efficacy. (A) Schematic illustration of treatment schedule and tumor growth of B16F10 tumor-bearing C57/BL6 mice ($n = 5$). Mice were intravenously administrated with saline, P-D-R8MTS (equivalent DOX dose 5 mg/kg), P-MSP-DMA (equivalent MSP dose 5 mg/kg) and SNV (equivalent DOX dose 5 mg/kg, MSP dose 5 mg/kg) on Days 8, 11, and 14. (B) Tumor inhibition rate of B16F10 tumors for each group harvested on Day 19 ($n = 5$). (C) Mice survival rate over time during the treatments ($n = 8$). (D) Analysis of CRT expression and (E) mature DCs infiltration and (F) PD-L1 expression after different treatments. Results were mean ± SEM ($n = 5$). * and ** indicated $P < 0.05$ and $P < 0.01$ *versus* control group, respectively. $^{\#}$ and $^{\#\#}$ indicated $P < 0.05$ and $P < 0.01$, respectively.

tumor accumulation of SNV-Cy5 was 7.69- and 2.91-fold higher than that of free Cy5 and P-D-R8MTS-Cy5, respectively (Fig. 5C and D). These results suggested SNV with certain particle size and shielding charge improved blood stability, which contributed to better tumor accumulation. Next, we evaluated whether SNV possessed pH-sensitive behavior after accumulating in tumors. P-D-R8MTS was labeled with Cy5 and P-MSP-DMA was labeled with Cy3. As shown in Supporting Information Fig. S9, at 1 h, the fluorescence of Cy5 and Cy3 was overlapped well, indicating most of SNV remained intact. As time prolonged to 4 h, some red fluorescence of Cy5 was separated from green Cy3, suggesting part of SNV was disassembled. Notably, after 8 h administration, most of red and green fluorescence was separated and distributed uniformly in tumors, demonstrating SNV was almost disintegrated. The above results confirmed that SNV exhibited pH-sensitive behavior to release P-D-R8MTS and P-MSP-DMA in tumors. Moreover, we investigated whether SNV was capable of delivering DOX to tumor mitochondria *in vivo*. B16F10 tumor-bearing C57/BL6 mice were intravenously administrated and tumor tissues were homogenized for flow cytometry analysis. The results indicated SNV remarkably increased DOX accumulation in tumor tissues, which was 2.96-fold higher than free DOX and 2.21-fold higher than P-D-R8MTS, respectively (Fig. 5E). Furthermore, we isolated mitochondria and found that the mitochondrial DOX accumulation of SNV was 11.98-fold higher than free DOX and 5.45-fold higher than P-D-R8MTS, respectively (Fig. 5F). The overall results confirmed that SNV was able to target tumor tissues and effectively deliver DOX to mitochondria for cancer elimination.

Subsequently, we evaluated *in vivo* therapeutic efficacy of SNV. B16F10 tumor-bearing C57/BL6 mice were intravenously administrated every 3 days for 3 rounds. Results in Fig. 6A and B and Supporting Information Fig. S10A showed that free DOX and P-MSP-DMA displayed slight tumor growth inhibition. In contrast, SNV exhibited superior antitumor capacity with a growth suppression rate of 80.73%, which was significantly higher than that of P-D-R8MTS (53.60%). This was mainly attributed to its improved tumor accumulation and mitochondrial targeting. Moreover, SNV remarkably prolonged the survival rate of mice with a median survival of 40 days compared to control (20.5 days) and other treatment (22.5−26 days) groups (Fig. 6C). The body weight change (Fig. S10B) and H&E staining (Fig. S10C) revealed that free DOX caused significant body weight loss and myocardial broken of mice, whereas no apparent body weight change and

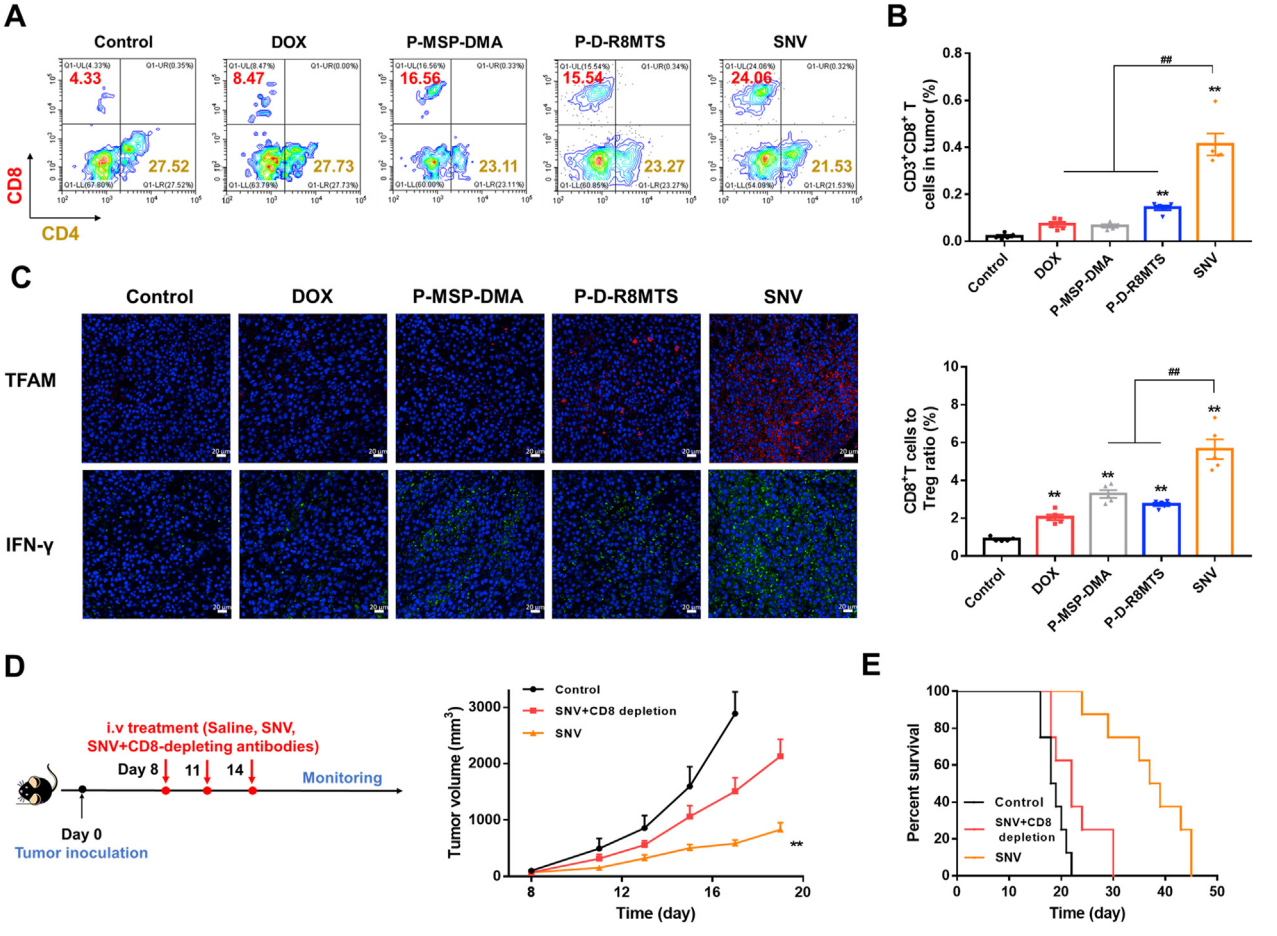

Figure 7 (A, B) Analysis of $CD3^+CD8^+$ T cells and $CD8^+$ T cells to Treg ratio after different treatments. Results were mean ± SEM ($n = 5$). (C) Immunofluorescence analysis of TFAM and IFN-γ expression in tumor. Blue: nucleus; Red: TFAM; Green: IFN-γ. Scale bar: 20 μm. Results were mean ± SEM ($n = 5$). ** indicated $P < 0.01$ *versus* control group. ## indicated $P < 0.01$. (D) Schematic illustration of treatment schedule and tumor growth curves of B16F10 tumor-bearing C57/BL6 mice. Mice were intravenously administrated with saline, SNV and SNV + CD8-delpeting antibodies on Days 8, 11, and 14. Results were mean ± SEM ($n = 5$). ** indicated $P < 0.01$ *versus* all other group. (E) Mice survival rate over time during the treatment ($n = 8$).

major organ injury was observed in copolymers and SNV group, demonstrating the safety of HPMA copolymer-based treatment.

Furthermore, we investigated whether SNV could augment *in vivo* immune responses. Tumors were homogenized on Day 19 and detected by flow cytometry. As expected, SNV considerably improved expression of CHOP, GRP78, P-ELF2α (Supporting Information Fig. S11A) and ecto-CRT (Fig. 6D) and promoted DCs infiltration (Fig. 6E) of B16F10 tumors, suggesting efficient ICD induction and phagocytosis with SNV administration. Consistent with *in vitro* results, DOX and P-D-R8MTS considerably raised PD-L1 level, a typical "don't eat me" signal to promote tumor cells to escape from immune surveillance, while P-MSP-DMA and SNV exhibited prominent downregulation of PD-L1 compared to control and P-D-R8MTS group (Fig. 6F). As a result, the activation of cytotoxic $CD8^+$ T cells in tumor infiltrating $CD3^+$ T cells was significantly increased from 5.82% (control group) to 24.71% after SNV treatment, while the proportion of immunosuppressive Treg cells was sharply declined (Fig. 7A and B, Fig. S11B and S11C). Moreover, immunofluorescence images revealed SNV intensively facilitated the secretion of mitochondria-associated TFAM in tumor, which stimulated antigen presentation to T cells, followed by enhanced release of interferon-γ (IFN-γ), the main cytotoxic cytokine of $CD8^+$ T cells to kill tumor (Fig. 7C). Meanwhile, immunosuppressive inflammatory cytokine Interleukin-6 (IL-6) was remarkably downregulated after SNV treatment as compared to all other groups (Fig. S10D)[34]. These results suggested SNV effectively improved antitumor immunity and alleviated immunosuppressive microenvironment.

To further verify the antitumor efficacy of SNV indeed depended on $CD8^+$ T lymphocytes but not just cytotoxicity of DOX, CD8-depleting antibodies were employed to eliminate $CD8^+$ T cells during SNV treatment in B16F10 tumor-bearing C57/BL6 mice (Fig. 7D). As expected, with $CD8^+$ T cells depletion, SNV-treated mice exhibited remarkably accelerated tumor growth and shortened survival rate (Fig. 7D and E). Taken together, SNV was able to suppress tumor progression through efficient immune activation and participation.

3.6. *Antitumor and anti-metastasis efficacy of SNV in metastatic 4T1 tumor model*

Moreover, we evaluated whether SNV could also achieve effective immune activation and antitumor efficacy in poorly immunogenic 4T1 tumors. Identical with the trends in B16F10 cells *in vitro*, SNV exhibited efficient mitochondrial targeting (Fig. 8A, Supporting Information Fig. S12) and ROS generation (Fig. 8B) in 4T1 cells. After 24 h incubation, SNV significantly facilitated surface CRT expression (Fig. 8C) and extracellular ATP release (Fig. 8D) as well as down-regulated PD-L1 level stimulated by P-D-R8MTS (Fig. 8E). These suggested SNV was capable of inducing ICD in low immunogenic 4T1 cells.

After that, we investigated *in vivo* immune responses in 4T1 tumor-bearing BALB/c mice. The *in vivo* biodistribution in 4T1 mice model demonstrated that SNV also exhibited significantly higher tumor accumulation than free Cy5 and P-D-R8MTS-Cy5 (Supporting Information Fig. S13), which was consistent with the results in B16 melanoma tumor model. After two doses administration, mice were sacrificed and tumors were homogenized for immunology analysis (Fig. 9A). Consistent with *in vitro* results, SNV triggered intensive ICD with enhanced CRT expression (Fig. 9B) and mature DCs infiltration (Fig. 9C) in tumor. Moreover, SNV prominently increased cytotoxic $CD8^+$ T cells infiltration and declined proportion of $CD4^+$ T and Treg cells (Fig. 9D and E, Supporting Information Fig. S14A and S14B). In addition, P-D-R8MTS largely up-regulated suppressive PD-L1 expression whereas SNV remained comparable to control group (Fig. 9F).

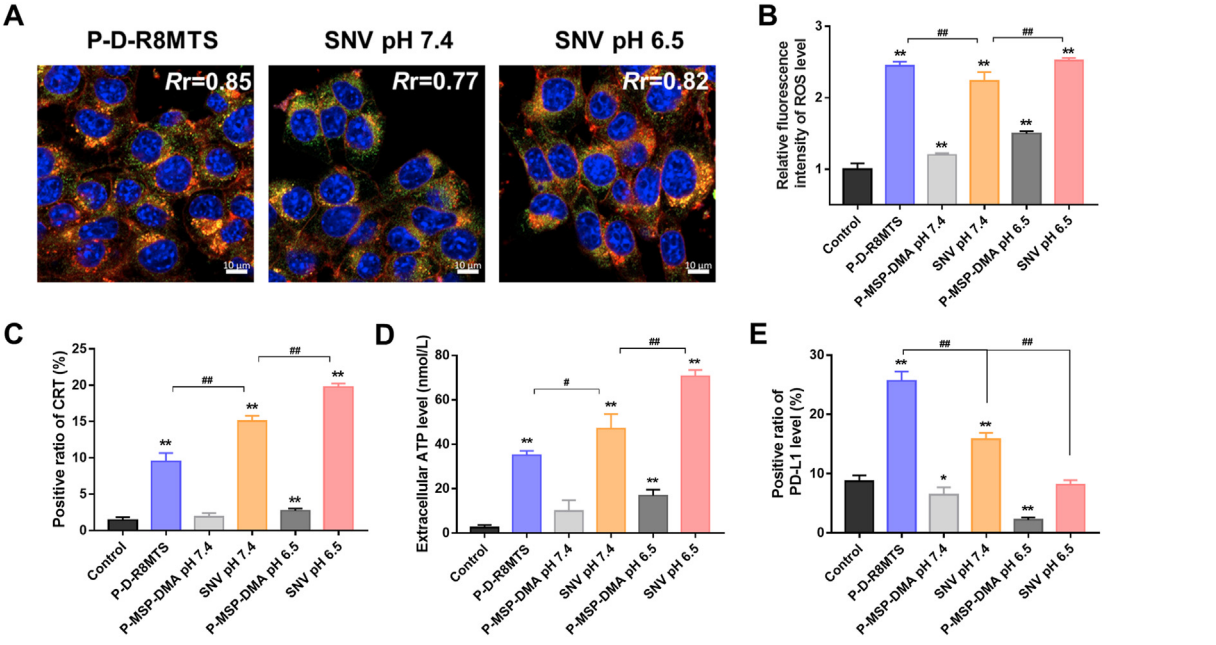

Figure 8 (A) Qualitative analysis of DOX accumulation in mitochondria of 4T1 cells by CLSM for 4 h. Blue: nucleus; Green: mitochondria; Red: DOX. Scale bar: 10 μm. Rr: Pearson correlation coefficient. (B) ROS level of 4T1 cells after treated with copolymers and SNV for 12 h. (C) Ecto-calreticulin, (D) extracellular ATP level and (E) PD-L1 level of 4T1 cells after treated with copolymers and SNV for 24 h. Results were mean ± SD ($n = 3$). * and ** indicated $P < 0.05$ and $P < 0.01$ *versus* control group, respectively. $^{\#}$ and $^{\#\#}$ indicated $P < 0.05$ and $P < 0.01$, respectively.

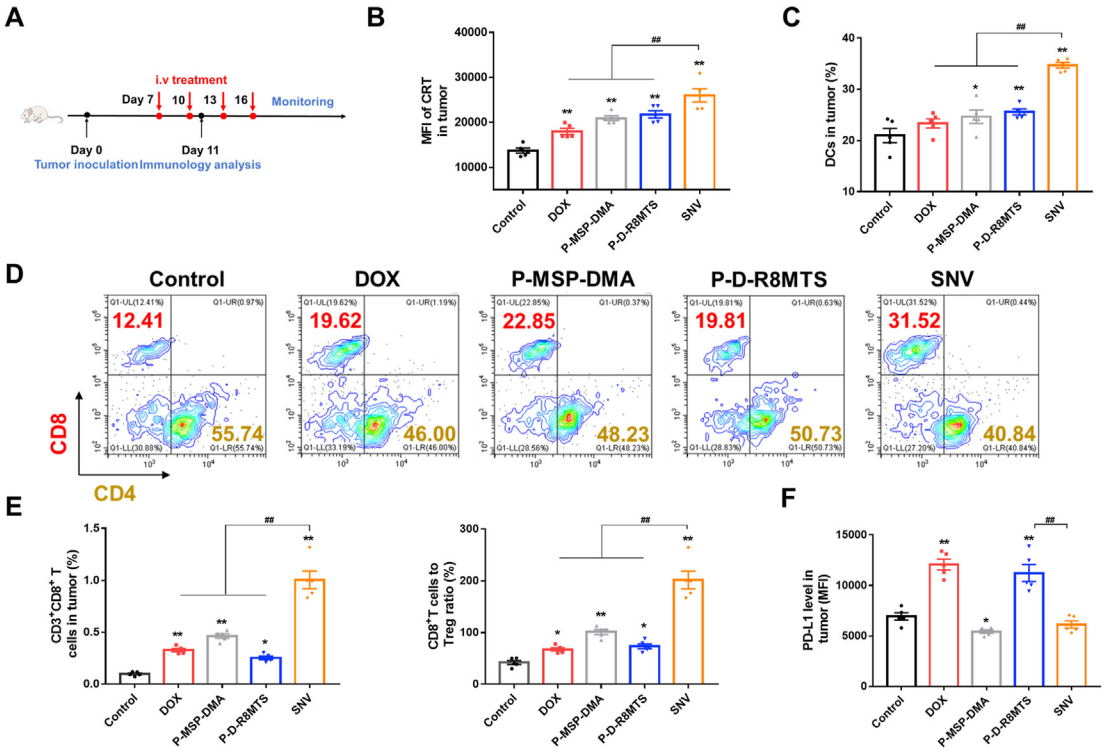

Figure 9 *In vivo* immune responses in 4T1 tumors. (A) Schematic illustration of treatment schedule in 4T1 tumor-bearing Balb/c mice. Mice were intravenously administrated with saline, P-D-R8MTS, P-MSP-DMA and SNV on Days 7, 10, 13 and 16. Immunology analysis was investigated on Day 11. (B) Analysis of CRT expression and (C) mature DCs infiltration after different treatments. (D, E) Analysis of $CD3^+CD8^+$ T cells and $CD8^+$ T cells to Treg ratio after different treatments. (F) PD-L1 expression after different treatments. Results were means ± SEM ($n = 5$). * and ** indicated $P < 0.05$ and $P < 0.01$ *versus* control group, respectively. $^{\#\#}$ indicated $P < 0.01$.

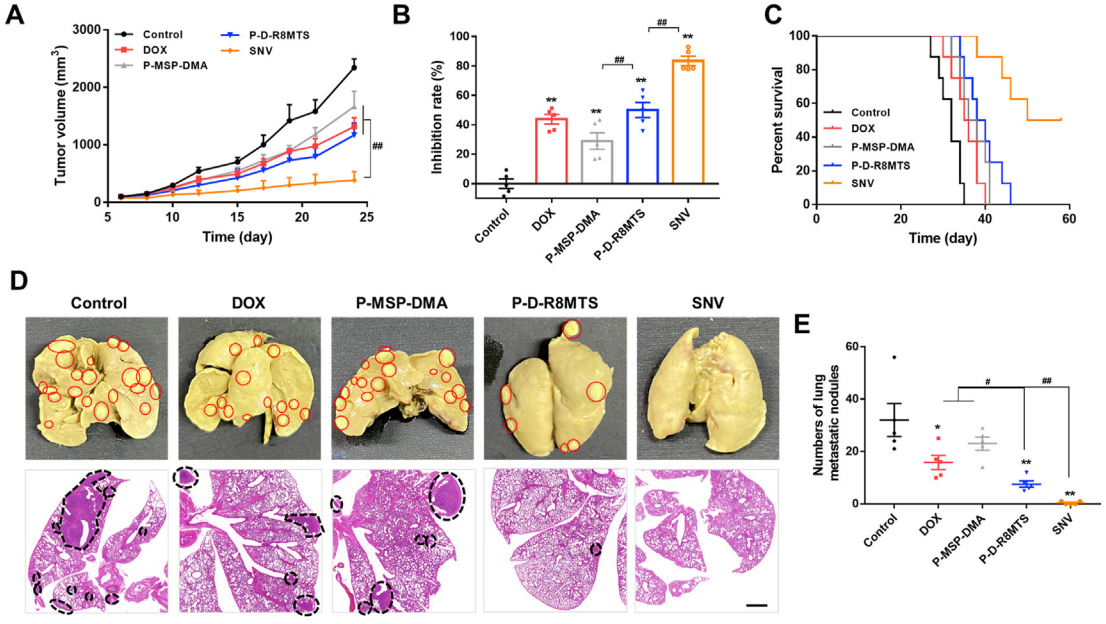

Figure 10 *In vivo* antitumor efficacy in 4T1 tumors. (A) Tumor growth and (B) tumor inhibition rate of 4T1 tumor-bearing Balb/c mice during treatment ($n = 5$). (C) Mice survival rate over time during the treatments ($n = 8$). (D) Representative image and HE staining of lungs and (E) quantitative analysis of lung metastatic nodules harvested on Day 24. Red and black circles indicated metastatic nodules. Scale bar: 500 μm. Results were mean ± SEM ($n = 5$). * and ** indicated $P < 0.05$ and $P < 0.01$ *versus* control group, respectively. $^{\#}$ and $^{\#\#}$ indicated $P < 0.05$ and $P < 0.01$, respectively.

These indicated SNV dominantly stimulated immune activation and alleviated immunosuppressive microenvironment. As a consequence, SNV exhibited the strongest tumor growth repression and the highest inhibition rate (83.48%) compared to other groups (28.98%−50.06%), and significantly prolonged survival of mice (Fig. 10A–C, Supporting Information Fig. S15A–S15C).

Furthermore, *in vivo* lung metastasis was also evaluated (Fig. 10D and E). Due to the limited antitumor efficacy, P-MSP-DMA failed to inhibit pulmonary metastasis of primary tumors. Interestingly, though free DOX and P-D-R8MTS showed comparable tumor growth suppression, the lung metastasis of P-D-R8MTS-treated mice was significantly restrained compared with free DOX. It was in line with our previous report that targeted delivering DOX to mitochondria could inhibit tumor metastasis efficiently[14]. Notably, SNV displayed the best anti-metastasis capability, with nearly no metastatic nodules and loci in lung (Fig. 10D and E). In addition, compared to tumor free mice, the infiltration of $CD8^+$ T cells from lungs of control group was significantly declined (Fig. S14C). However, after SNV treatment, the infiltration of $CD8^+$ T cells was enhanced. Moreover, the massive lung metastasis of control group led to up-regulation of PD-L1, whereas SNV remarkably downregulated the PD-L1 level in lung. These findings demonstrated SNV was able to recruit/revive the $CD8^+$T cells and mitigate the immunosuppressive microenvironment in distant lung to inhibit pulmonary metastasis. To sum up, the above results indicated SNV was able to activate immune responses in low immunogenic 4T1 tumors as well, resulting in effective tumor suppression and anti-metastasis efficacy.

4. Conclusions

To date, majority of ICD-inducing approaches concentrate on enhancing delivery of ICD inducers to tumor tissues, with less attention paid to further sub-organelle targeted delivery[35−37]. A few studies have focused on ER-targeted drug delivery owing to the close association between ER stress and ICD[38−40]. Here, our pioneering work also revealed that mitochondria-targeted delivery of anthracycline drug to promote ROS generation was an effective strategy for robust ICD induction. Targeted mitochondrial damage by P-D-R8MTS triggered substantial generation of ROS, which consequently resulted in elicitation of ER stress and release of mitochondria-associated damage molecules. As a result, direct ICD induction was amplified. Nevertheless, two challenges remained to be addressed: (1) the cationic charge of P-D-R8MTS severely limited its tumor accumulation due to rapid clearance by reticuloendothelial system; (2) chemotherapy could negatively regulate the immunosuppressive microenvironment by upregulating PD-L1 to help the tumor evade the host immune system.

To overcome such obstacles, here we developed a novel multifunctional self-assembled nano vehicle (SNV) capable of mitochondrial targeted ICD induction and PD-L1 blockade. The anionic PD-L1 blocking copolymer P-MSP-DMA shielded the cationic charge of P-D-R8MTS, not only facilitating the tumor accumulation and mitochondrial targeting of SNV, but also allowing the simultaneous accumulation of PD-L1 antagonistic peptide (MSP) and doxorubicin (DOX) in tumor site. On one aspect, P-D-R8MTS targeted and destroyed mitochondria to promote substantial ROS generation, resulting in massively amplified ICD *via* two pathways: (1) ROS elevated ER stress, leading to surface exposure of calreticulin; (2) ROS induced apoptosis to promote release of mitochondria-associated damage molecules (including mitochondrial transcription factor A and ATP) as well as HMGB1. On another aspect, P-MSP-DMA reversed the up-regulation of PD-L1 stimulated by P-D-R8MTS to mitigate tumor immunosuppression and unleashing the killing effect of $CD8^+$ T cells. As a consequence, SNV significantly promoted antitumor immune responses and antitumor efficacy in B16F10 melanoma and low immunogenic 4T1 breast cancer, and suppressed pulmonary metastasis of orthotopic 4T1 tumor. Overall, our work provides a novel, generalizable approach to enhance cancer immunotherapy by coordinating mitochondrial-targeted ICD induction and PD-L1 blockade.

Acknowledgements

The authors gratefully acknowledge financial support from the National Natural Science Foundation for Distinguished Young Scholars (81625023, China).

Author contributions

Qiuyi Li carried out the experiments, analyzed data and drafted the manuscript. Cheng Chen, Jinxia Kong and Junlin Li participated a part of the experiments. Lian Li contributed to paper revision. Yuan Huang came up with ideas, wrote and polished this manuscript and was responsible for supervision. All of the authors have read and approved the final manuscript.

Conflicts of interest

The authors declare no competing financial interests.

Appendix A. Supporting information

Supporting data to this article can be found online at https://doi.org/10.1016/j.apsb.2021.11.005.

References

1. Wellenstein MD, de Visser KE. Cancer-cell-intrinsic mechanisms shaping the tumor immune landscape. *Immunity* 2018;**48**:399−416.
2. Hurwitz AA, Watkins SK. Immune suppression in the tumor microenvironment: a role for dendritic cell-mediated tolerization of T cells. *Cancer Immunol Immunother* 2012;**61**:289−93.
3. Krysko DV, Garg AD, Kaczmarek A, Krysko O, Agostinis P, Vandenabeele P. Immunogenic cell death and DAMPs in cancer therapy. *Nat Rev Cancer* 2012;**12**:860−75.
4. Garg AD, Agostinis P. ER stress, autophagy and immunogenic cell death in photodynamic therapy-induced anti-cancer immune responses. *Photochem Photobiol Sci* 2014;**13**:474−87.
5. Yin YF, Jiang XW, Sun LP, Li HY, Su CX, Zhang Y, et al. Continuous inertial cavitation evokes massive ROS for reinforcing sonodynamic therapy and immunogenic cell death against breast carcinoma. *Nano Today* 2021;**36**:101009.
6. Zheng P, Ding BB, Jiang ZY, Xu WG, Li G, Ding JX, et al. Ultrasound-augmented mitochondrial calcium ion overload by calcium nanomodulator to induce immunogenic cell death. *Nano Lett* 2021;**21**:2088−93.
7. Fulda S, Galluzzi L, Kroemer G. Targeting mitochondria for cancer therapy. *Nat Rev Drug Discov* 2010;**9**:447−64.
8. Wang Y, Luo SL, Zhang C, Liao XY, Liu T, Jiang ZY, et al. An NIR-fluorophore-based therapeutic endoplasmic reticulum stress inducer. *Adv Mater* 2018:e1800475.
9. Chen C, Ni X, Jia SR, Liang Y, Wu X, Kong DL, et al. Massively evoking immunogenic cell death by focused mitochondrial oxidative

stress using an AIE luminogen with a twisted molecular structure. *Adv Mater* 2019;**31**:1904914.
10. Jeong SD, Jung BK, Ahn HM, Lee DY, Ha JH, Noh I, et al. Immunogenic cell death inducing fluorinated mitochondria-disrupting helical polypeptide synergizes with PD-L1 immune checkpoint blockade. *Adv Sci* 2021;**8**:2001308.
11. Yang MH, Li CF, Zhu S, Cao LZ, Kroemer G, Zeh H, et al. TFAM is a novel mediator of immunogenic cancer cell death. *Oncoimmunology* 2018;**7**:e1431086.
12. Galluzzi L, Kepp O, Kroemer G. Mitochondria: master regulators of danger signalling. *Nat Rev Mol Cell Biol* 2012;**13**:780−8.
13. Rodríguez-Nuevo A, Zorzano A. The sensing of mitochondrial DAMPs by no*N*-immune cells. *Cell Stress* 2019;**3**:195.
14. Li QY, Yang JT, Chen C, Lin X, Zhou ML, Zhou Z, et al. A novel mitochondrial targeted hybrid peptide modified HPMA copolymers for breast cancer metastasis suppression. *J Control Release* 2020;**325**:38−51.
15. Samanta D, Park Y, Ni X, Li H, Zahnow CA, Gabrielson E, et al. Chemotherapy induces enrichment of $CD47^+/CD73^+/PDL1^+$ immune evasive triple-negative breast cancer cells. *Proc Natl Acad Sci U S A* 2018;**115**:E1239−48.
16. Li L, Li YC, Yang CH, Radford DC, Wang JW, Janát-Amsbury M, et al. Inhibition of immunosuppressive tumors by polymer-assisted inductions of immunogenic cell death and multivalent PD-L1 cross-linking. *Adv Funct Mater* 2020;**30**:1908961.
17. Wang TY, Wu XX, Guo CY, Zhang KJ, Xu JY, Li Z, et al. Development of inhibitors of the programmed cell death-1/programmed cell death-ligand 1 signaling pathway. *J Med Chem* 2019;**62**:1715−30.
18. Shaabani S, Huizinga HPS, Butera R, Kouchi A, Guzik K, Magiera-Mularz K, et al. A patent review on PD-1/PD-L1 antagonists: small molecules, peptides, and macrocycles (2015–2018). *Expert Opin Ther Pat* 2018;**28**:665−78.
19. Rani S, Gupta U. HPMA-based polymeric conjugates in anticancer therapeutics. *Drug Discov Today* 2020;**25**:997−1012.
20. Chytil P, Kostka L, Etrych T. HPMA copolymer-based nanomedicines in controlled drug delivery. *J Pers Med* 2021;**11**:115.
21. Ulbrich K, Subr V, Strohalm J, Plocova D, Jelınkova M, Rihova B. Polymeric drugs based on conjugates of synthetic and natural macromolecules: I. Synthesis and physico-chemical characterisation. *J Control Release* 2000;**64**:63−79.
22. Liu X-M, Quan L-D, Tian J, Alnouti Y, Fu K, Thiele GM, et al. Synthesis and evaluation of a well-defined HPMA copolymer−dexamethasone conjugate for effective treatment of rheumatoid arthritis. *Pharm Res* 2008;**25**:2910−9.
23. Tang JY, Ou-Yang F, Hou MF, Huang HW, Wang HR, Li KT, et al. Oxidative stress-modulating drugs have preferential anticancer effects—involving the regulation of apoptosis, DNA damage, endoplasmic reticulum stress, autophagy, metabolism, and migration. *Semin Cancer Biol* 2019;**58**:109−17.
24. Bhandary B, Marahatta A, Kim HR, Chae HJ. An involvement of oxidative stress in endoplasmic reticulum stress and its associated diseases. *Int J Mol Sci* 2012;**14**:434−56.
25. Bhat TA, Chaudhary AK, Kumar S, O'Malley J, Inigo JR, Kumar R, et al. Endoplasmic reticulum-mediated unfolded protein response and mitochondrial apoptosis in cancer. *Biochim Biophys Acta Rev Cancer* 2017;**1867**:58−66.
26. Oresta B, Pozzi C, Braga D, Hurle R, Lazzeri M, Colombo P, et al. Mitochondrial metabolic reprogramming controls the induction of immunogenic cell death and efficacy of chemotherapy in bladder cancer. *Sci Transl Med* 2021;**13**.
27. Phung CD, Nguyen HT, Choi JY, Pham TT, Acharya S, Timilshina M, et al. Reprogramming the T cell response to cancer by simultaneous, nanoparticle-mediated PD-L1 inhibition and immunogenic cell death. *J Control Release* 2019;**315**:126−38.
28. Li CL, Zhang NP, Zhou JD, Ding C, Jin YQ, Cui XY, et al. Peptide blocking of PD-1/PD-L1 interaction for cancer immunotherapy. *Cancer Immunol Res* 2018;**6**:178−88.
29. Nakase I, Niwa M, Takeuchi T, Sonomura K, Kawabata N, Koike Y, et al. Cellular uptake of arginine-rich peptides: roles for macropinocytosis and actin rearrangement. *Mol Ther* 2004;**10**:1011−22.
30. El-Sayed A, Khalil IA, Kogure K, Futaki S, Harashima H. Octaarginine- and octalysine-modified nanoparticles have different modes of endosomal escape. *J Biol Chem* 2008;**283**:23450−61.
31. Escors D, Gato-Canas M, Zuazo M, Arasanz H, Garcia-Granda MJ, Vera R, et al. The intracellular signalosome of PD-L1 in cancer cells. *Signal Transduct Target Ther* 2018;**3**:26.
32. Li J, Chen L, Xiong Y, Zheng X, Xie Q, Zhou Q, et al. Knockdown of PD-L1 in human gastric cancer cells inhibits tumor progression and improves the cytotoxic sensitivity to CIK therapy. *Cell Physiol Biochem* 2017;**41**:907−20.
33. Saleh R, Taha RZ, Sasidharan Nair V, Alajez NM, Elkord E. PD-L1 blockade by atezolizumab downregulates signaling pathways associated with tumor growth, metastasis, and hypoxia in human triple negative breast cancer. *Cancers* 2019;**11**:1050.
34. Wang D, DuBois RN. Immunosuppression associated with chronic inflammation in the tumor microenvironment. *Carcinogenesis* 2015;**36**:1085−93.
35. Zhou ML, Luo CH, Zhou Z, Li L, Huang Y. Improving anti-PD-L1 therapy in triple negative breast cancer by polymer-enhanced immunogenic cell death and CXCR4 blockade. *J Control Release* 2021;**334**:248−62.
36. Wei BC, Pan JM, Yuan RT, Shao BF, Wang Y, Guo X, et al. Polarization of tumor-associated macrophages by nanoparticle-loaded *Escherichia coli* combined with immunogenic cell death for cancer immunotherapy. *Nano Lett* 2021;**21**:4231−40.
37. Huang ZS, Wang YX, Yao D, Wu JH, Hu YQ, Yuan AH. Nanoscale coordination polymers induce immunogenic cell death by amplifying radiation therapy mediated oxidative stress. *Nat Commun* 2021;**12**:1−18.
38. Deng HZ, Zhou ZJ, Yang WJ, Lin LS, Wang S, Niu G, et al. Endoplasmic reticulum targeting to amplify immunogenic cell death for cancer immunotherapy. *Nano Lett* 2020;**20**:1928−33.
39. Li J, Gao H, Liu R, Chen C, Zeng S, Liu Q, et al. Endoplasmic reticulum targeted AIE bioprobe as a highly efficient inducer of immunogenic cell death. *Sci China Chem* 2020;**63**:1428−34.
40. Wang LL, Guan RL, Xie LN, Liao XX, Xiong K, Rees TW, et al. An ER-targeting iridium (III) complex that induces immunogenic cell death in non-small-cell lung cancer. *Angew Chem* 2021;**133**:4707−15.